International Journal of Machine Tools & Manufacture 162 (2021) 103688

Contents lists available at ScienceDirect

International Journal of Machine Tools and Manufacture

journal homepage: http://www.elsevier.com/locate/ijmactool

Chip-free surface patterning of toxic brittle polycrystalline materials through micro/nanoscale burnishing

Weihai Huang, Jiwang Yan *

Department of Mechanical Engineering, Faculty of Science and Technology, Keio University, 3-14-1 Hiyoshi, Kohoku-ku, Yokohama, 223-8522, Japan

ARTICLE INFO

Keywords:
Micro/nano machining
Burnishing
Soft brittle material
Poly crystal
Subsurface damage
Surface patterning

ABSTRACT

Brittle crystalline materials have important applications in optics and optoelectronics. However, their powders are highly toxic; thus, the chips generated in material removal processes such as cutting, grinding, and polishing are harmful to human health and the environment. In this study, micro/nanoscale burnishing tests were conducted on polycrystalline zinc selenide (*p*-ZnSe) to explore the feasibility of high-precision surface patterning of a toxic material by local plastic deformation without chip generation. The local deformation behaviours and subsurface damage formation mechanisms were investigated under dry and oil-lubricated conditions. Two types of cracks occurred when the force exceeded a critical value: cracks along the slip planes at the groove bottom and cracks along the cleavage planes at the groove edge. Below the critical force value, however, a crack-free surface was obtained with lower surface roughness than those for diamond-turned surfaces. No phase transformation was detected after burnishing, but lattice distortion appeared in the subsurface layer. A model was developed to predict the activated slip planes by calculating the maximum Schmid factors of the slip systems, and the distribution of subsurface defects was clarified by cross-sectional direct observations. It was also found that the use of a lubricating oil could greatly reduce material pile-ups around the tool. As test pieces, microgrid patterns were fabricated by crossing and overlapping the grooves, and smooth surfaces with surface roughness of 1.85 nm Sa and 4.5 nm Sa, respectively, were achieved. The findings from this study demonstrate the feasibility of chip-free surface patterning on toxic brittle polycrystalline materials by micro/nanoscale burnishing, which is an effective alternative to cutting and grinding for the fabrication of micro structured optical elements and microfluidics.

1. Introduction

Various brittle crystalline materials are used extensively in optical, optoelectronic, biomedical, and semiconductor applications. Several examples are as follows: monocrystalline/polycrystalline Ge is a popular material for thermography lenses [1]; single-crystal potassium dihydrogen phosphate (KDP) is widely used in the laser-driven inertial confinement fusion facilities [2]; single-crystal Ga_2O_3 is a promising material for high power electronic devices and solar-blind ultraviolet (UV) photodetectors [3]; single-crystal Lu_2O_3 is an emerging laser crystal material for high-power solid state lasers [4]; single-crystal CaF_2 is widely used as achromatic lenses in high-end cameras, photolithography lenses, and micro fluidics for protein analysis [5]; polycrystalline ZnSe is an attractive infrared (IR) optical material used for night vision systems of autonomous vehicles and windows of high-power carbon dioxide lasers [6].

A common feature of these materials is their low fracture toughness, which makes them very difficult to machine. Surface and subsurface microfractures can easily occur when machining these materials under conventional conditions [7]. In some strictly controlled conditions, ductile machining can be realised by ultraprecision diamond turning [8], micro end milling [9], and micro grinding [10] to achieve optical-quality surfaces on these materials.

Another critical issue in manufacturing components of these brittle crystalline materials using material removal processes, such as cutting, grinding, and polishing, is chip disposal. Submicron scale powder-type chips generated in such material removal processes are easily inhaled and cause severe health hazards to operators. For example, subclinical glomerular change is likely to occur among the workers who are exposed to Ge powder [11]; KDP chips have shown symptoms of somnolence (general depressed activity) and functional changes in the gastrointestinal system [12]; Ga_2O_3 chips cause alveolar histiocytosis and septal fibrosis [13]; Lu_2O_3 chips may cause serious eye and skin irritation as well as respiratory irritation [14]; CaF_2 chips affect fertility, change

* Corresponding author.
E-mail address: yan@mech.keio.ac.jp (J. Yan).

https://doi.org/10.1016/j.ijmachtools.2020.103688
Received 21 October 2020; Received in revised form 23 December 2020; Accepted 27 December 2020
Available online 2 January 2021

teeth and supporting structures, and induce a change in blood or tissue levels [15]. In particular, ZnSe powder has acute toxicity. Inhaling or exposure to ZnSe powder leads to severe organ damage [16].

To reduce or prevent chip pollution in the machining of toxic materials, special chip collection systems and cleaning units must be equipped with machine tools, which greatly increases the production costs and process complexity; even then, the health risk to operators still exists. From this point of view, an alternative manufacturing process without chip generation is needed to process these materials.

Burnishing is a surface finishing method that plastically deforms the surface of a workpiece by sliding a ball-shaped tool against the workpiece [17,18]. This method is effective for modifying metal surfaces by enhancing surface smoothness, wear resistance, and corrosion resistance; closing porosity; and creating compressive residual stresses [19,20]. More importantly, no chips are generated during burnishing. Hence, this process might be useful for machining toxic materials by avoiding potential threats from chip disposal. However, to date, the literature on burnishing brittle crystalline materials, such as ZnSe, is extremely limited; thus, the feasibility of burnishing such materials in a ductile mode, that is, plastically deforming the surface layer of a brittle crystalline material, is still unclear.

Conventional burnishing is usually performed using a ball tool with a millimetre-level radius, and the burnishing depth is controlled at a few tens of microns [18]. Apparently, such conditions cannot be used for burnishing brittle materials such as ZnSe, because they will lead to catastrophic fractures to the workpiece. Therefore, a far smaller radius tool and a far smaller burnishing depth are necessary for soft and brittle materials. Burnishing under such conditions is geometrically similar to scratching, where a stylus tool with a smaller radius (several to tens of microns) is used at a smaller depth (~a few microns). From this point of view, understanding the scratching phenomenon of a material may help to clarify the mechanism of burnishing ZnSe and other brittle materials.

Although there has been an abundant amount of literature on scratching of various materials, to the best of our knowledge, no study has been reported to date on the scratching behaviour of ZnSe. Existing literature on the deformation behaviour of ZnSe is based on indentation experiments and characterisation of hardness, fracture toughness, creep response [21], mechanical strength at elevated temperatures [22], and pressure-induced phase transformation [23], the mechanisms of which are different from those of burnishing in terms of the tool-workpiece interaction. In addition, most ZnSe optical components are polycrystalline ZnSe (*p*-ZnSe), the grain size of which is dozens of microns, grown by chemical vapour deposition (CVD) technology [24]. Hence, it is important to clarify the deformation behaviour of *p*-ZnSe during scratching and burnishing, specifically at a depth of micro/nanometre scale.

In this study, micro/nanoscale burnishing of *p*-ZnSe was attempted using a high-precision scratching apparatus, and the mechanisms of material plastic deformation and subsurface damage formation behaviours were investigated under dry and oil-lubricated conditions. The dependence of the surface defects on the crystal grain orientations was predicted using an analytical model. The distribution of subsurface defects and the role of the grain boundary were observed by cross-sectional transmission electron microscopy (XTEM) and electron backscatter diffraction (EBSD). Finally, two types of micropatterns were fabricated to demonstrate the feasibility of fabricating high-precision structured surfaces by burnishing. The findings from this study will not only assist in understanding the material deformation behaviours of *p*-ZnSe associated with crystal orientation, grain boundary, and interfacial lubrication, but also demonstrate the possibility of manufacturing microstructured surfaces on various toxic brittle polycrystalline materials without chip generation.

2. Material and methods

A double-side polished *p*-ZnSe cylinder (diameter: 25 mm, thickness: 3 mm) was used as the workpiece, the mean surface roughness (Sa) of which was less than 5 nm in a field of 200 × 200 μm^2. The workpiece material was prepared by the CVD method, and the grain size ranged from 3 to 80 μm. The properties of the workpiece are summarised in Table 1.

Burnishing tests were conducted under a force-control mode using a nanoindentation-scratching system, Nano Indenter G200 (KLA Corp., USA). The displacement resolution and force resolution of the indentation head were 0.01 nm and 50 nN, respectively. The scratch speed could be set within the range of 100 nm/s–2 mm/s. The passive negative-stiffness vibration isolation platform, BM-8 (Minus K Technology Inc., USA) provides vibration isolation in both vertical and horizontal directions. A photograph of the main section of the experimental system is shown in Fig. 1(a). A conical diamond stylus tool with a spherical tip was used for burnishing. Fig. 1(b) and (c) present an SEM general view and a close-up view of the tool tip, respectively. The apex angle of the tool was 90°, and the tip radius was 10 μm. The adhesion seen around the tool tip is contamination which could not be washed away during cleaning. Although the contamination may slightly affect the burnishing process at a very early stage, it will be removed soon after the tool-workpiece contact, thus will not have significant impact to the subsequent burnishing process. This is verified by the fact that there are no scratches on the groove surface caused by the contamination. To investigate the effect of lubrication on the deformation behaviour of the material, burnishing tests were performed under both dry and oil-lubricated conditions, where a lubricating oil, Shell Tellus Oil ST 32 (Showa Shell Sekiyu K.K.), was applied to the workpiece before the burnishing test. For each condition, three burnishing tests were conducted at constant normal forces of 2, 5, and 10 mN, respectively. During each burnishing test, the tool scanned the workpiece along the same path three times: (1) the tool probed the surface under an extremely small normal force (<7 μN) at a velocity of 10 μm/s to detect the original topography; (2) the tool burnished the surface under the pre-determined normal force at a velocity of 1 μm/s; and (3) the tool probed the surface under the same conditions as those in step (1) to detect the resulting surface profile. Fig. 2 schematically shows these three process steps. The experimental parameters for the burnishing tests are summarised in Table 2.

After the burnishing tests, the burnished grooves were characterised using an atomic force microscope (AFM), AFM5100 N (Hitachi High-Technologies Corp., Japan). The grooves were observed using a field-emission scanning electron microscope (FE-SEM), ZEISS MERLIN Compact (Carl Zeiss AG, Germany). There is no need to apply an electrically conductive coating to the sample surface before FE-SEM observation, so that nanoscale surface features can be directly observed without coating-induced topographical changes. Thereafter, a laser micro Raman spectroscope, inVia Raman (Renishaw Plc., UK), was used to analyse the microstructural change in the workpiece subsurface layer. To further understand the material deformation behaviour related to crystallographic orientation, the subsurface microstructure of a groove was characterised using an FE-SEM ZEISS GeminiSEM 500 (Carl Zeiss AG, Germany) equipped with an EBSD detector (EDAX Inc., USA). Moreover, a cross-sectional specimen of a groove along the burnishing direction was prepared using a Quanta 3D FEG SEM/FIB (focussed ion beam) system (FEI Company, USA), and was characterised by a TEM Tecnai G2 (FEI Company, USA) and EBSD analysis. The two types of microstructure patterns created by burnishing were measured using a

Table 1
Properties of the workpiece.

Material	Polycrystalline ZnSe
Grain size	3–80 μm
Hardness	1.6 ± 0.3 GPa
Young's modulus	70 ± 2 GPa
Poisson ratio	0.28

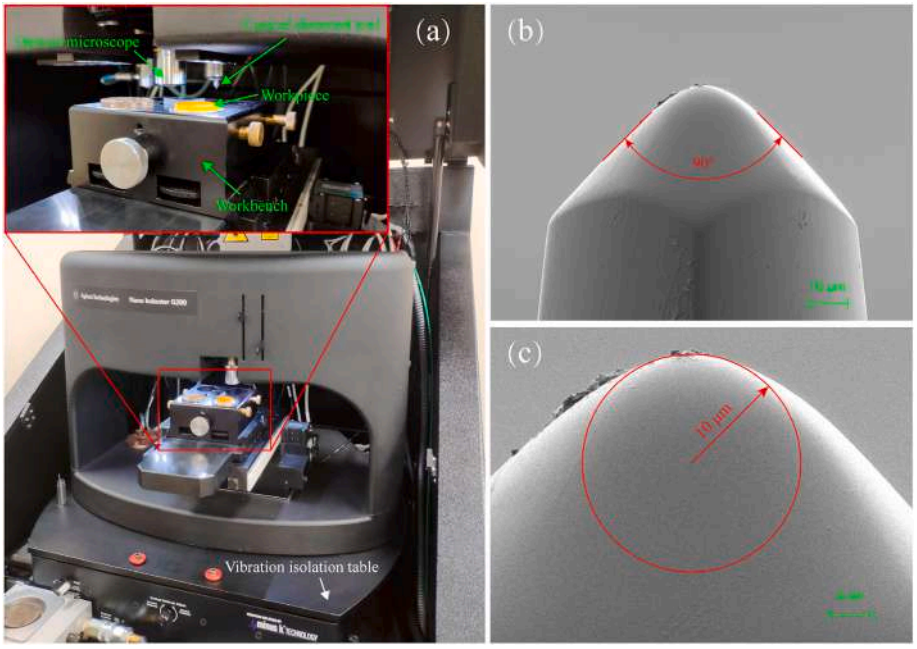

Fig. 1. (a) Photograph of the nanoindentation and scratching system used for burnishing test. SEM images of the (b) general view of the conical diamond tool; (c) close-up view of the tool tip.

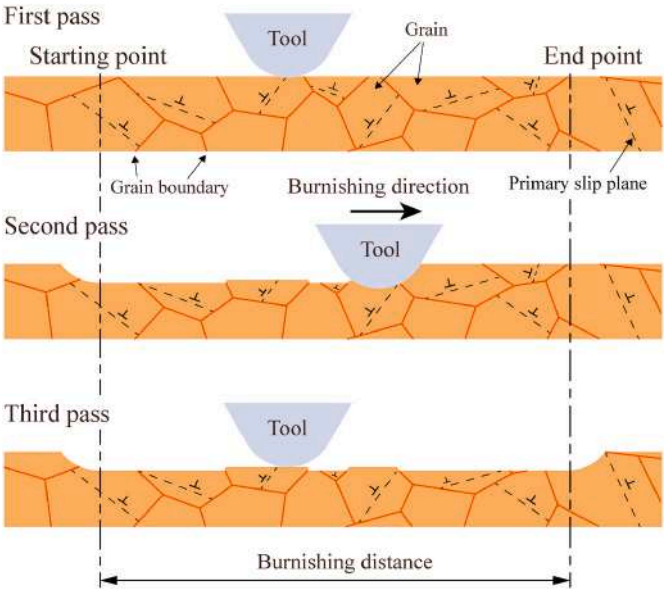

Fig. 2. Schematic diagram of the three process steps of the burnishing test.

Table 2
Experimental parameters used in the burnishing tests.

Parameters	Value
Tool tip	Spherical (radius = 10 μm)
Burnishing parameters	
Load (normal force)	2, 5, 10 mN
Speed	1 μm/s
Environment	
Lubrication condition	Dry and lubricating oil
Temperature	23 °C

Talysurf CCI 1000 white light interferometer (Taylor Hobson Ltd., UK).

3. Results and discussions

3.1. Surface morphology under dry conditions

The morphologies of the grooves burnished under dry conditions at three different constant forces were examined by SEM, as presented in Figs. 3–5. At a force of 2 mN, the entire groove is shown in Fig. 3(a). To further observe the features of different burnishing regions, close-up views of the regions marked in Fig. 3(a), which correspond to the beginning, middle, and end parts of the burnished groove, are presented in Fig. 3(b), (c), and (d), respectively. It can be observed that the groove was smooth without any burnishing-induced surface cracks, and only a few slip lines formed in the groove, as indicated by the arrows in Fig. 3 (b). The edge of the burnished groove was intact, indicating that the material underwent elastic–plastic deformation [25]. It is also observed that there are many intrinsic scratches on the workpiece surface which were generated by mechanical polishing during the sample preparation process. It is worth noting that those intrinsic scratches on the workpiece surface partially remained in the burnished groove. This indicates that no material was removed from the workpiece surface and that the material underwent plastic flow during the burnishing process. The fact that the intrinsic scratches became shallower after burnishing indicates that the plastic flow took place at the nanometre scale. Through the micro/nanoscale material flow, the burnished surface becomes smoother than the starting surface. The intrinsic scratches did not affect the observation of the slip lines, as the scratches are long and deep, crossing in random directions; whereas the slip lines are short and shallow, running in parallel directions.

For the groove burnished at a force of 5 mN, as shown in Fig. 4, the width of the groove was larger than that shown in Fig. 3. From the close-up views, it can be observed that more slip lines appeared at the bottom of the groove along the burnishing direction, indicating that the material was plastically deformed to a greater extent. Moreover, several cracks formed in the groove (see Fig. 4(c)). The cracks were not parallel to the slip lines, and some cracks were only generated at the groove edge. This phenomenon will be further discussed in Section 3.6. In addition, the intrinsic scratches on the workpiece surface can still be observed in the

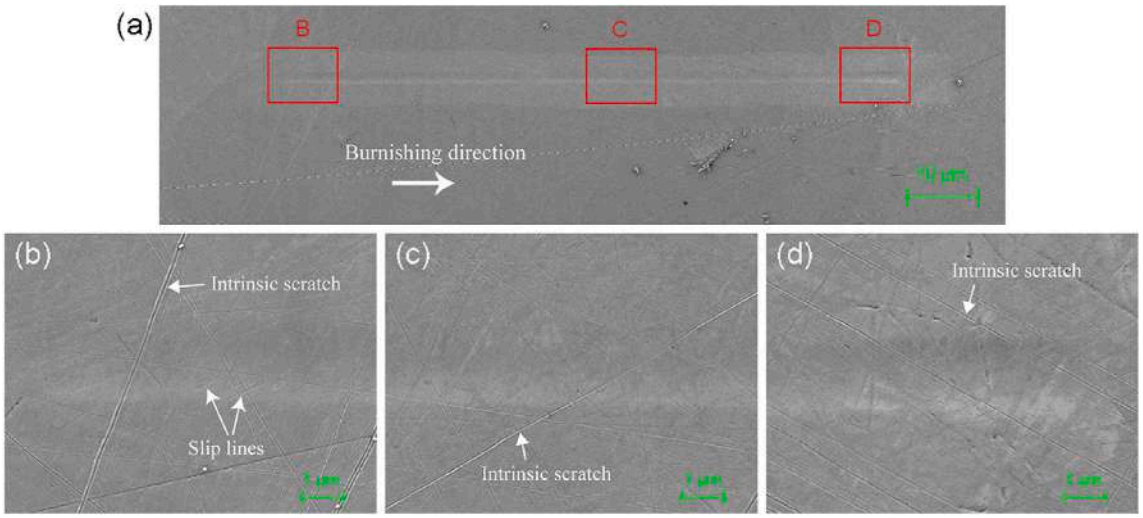

Fig. 3. SEM images of (a) burnished groove under the force of 2 mN with dry conditions; (b–d) corresponding close-up views of the regions, which were indicated by B, C, and D in (a).

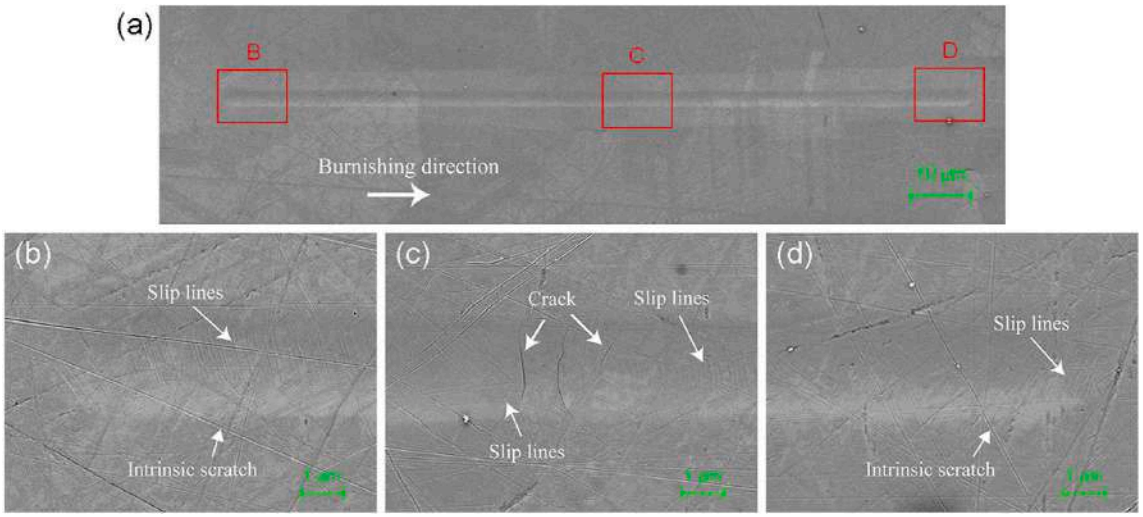

Fig. 4. SEM images of (a) burnished groove under the force of 5 mN with dry conditions; (b–d) corresponding close-up views of the regions, which were indicated by B, C, and D in (a).

groove.

When the force was increased to 10 mN, more cracks appeared in the burnished groove, as shown in Fig. 5. In the close-up views, cracks were parallel to the slip lines at the groove bottom, but deflected by an angle when it propagated to the groove edge. Additionally, the crack densities, in terms of the number of cracks per unit area, were different in grains with varied crystallographic orientations. From Fig. 5(c), it can be observed that the slip lines formed not only at the groove bottom but also at the groove edge. The slip lines of the groove bottom and groove edge were in different directions, indicating that two slip systems were activated. The activation of slip systems and the formation of cracks, which were dominated by the grain orientation and stress fields, will be discussed in Sections 3.5 and 3.6, respectively. It is worth mentioning that at the groove edge, the cracks passed across the slip lines without disturbing the propagation of the slip lines. This indicates that crack initiation occurred after the formation of slip lines. This may be because the cracks were caused by the tensile stress generated during material elastic recovery after the tool had passed through. A pile-up was found at the end of the groove, as shown in Fig. 5(d). In addition, it can be observed that the slip line emanated from the pile-up, which implies that as the tool moved forward, the pile-up in front of the tool was pushed aside, resulting in the formation of slip lines at the groove edge. Nevertheless, material removal from the workpiece surface did not occur during the burnishing process because the intrinsic scratches of the workpiece surface remained in the groove.

3.2. *Surface morphology under lubricated conditions*

Figs. 6–8 show the SEM images of the grooves burnished under lubricated conditions at the same forces as those used under dry conditions. Fig. 6 presents the groove burnished at 2 mN. In the close-up view of the groove, although many intrinsic scratches were found in the groove, neither cracks nor slip lines were observed.

Fig. 7 shows the groove burnished at a force of 5 mN under lubricated conditions. Only a few cracks were observed in the burnished groove. It is worth noting, however, that several intrinsic scratches of the workpiece surface vanished, as indicated by the arrows in Fig. 7(c) and (d). Because no fresh surface caused by material removal has been created, it is supposed that the vanishing of the intrinsic scratches was caused by burnishing; that is, the surface layer of the workpiece was plastically

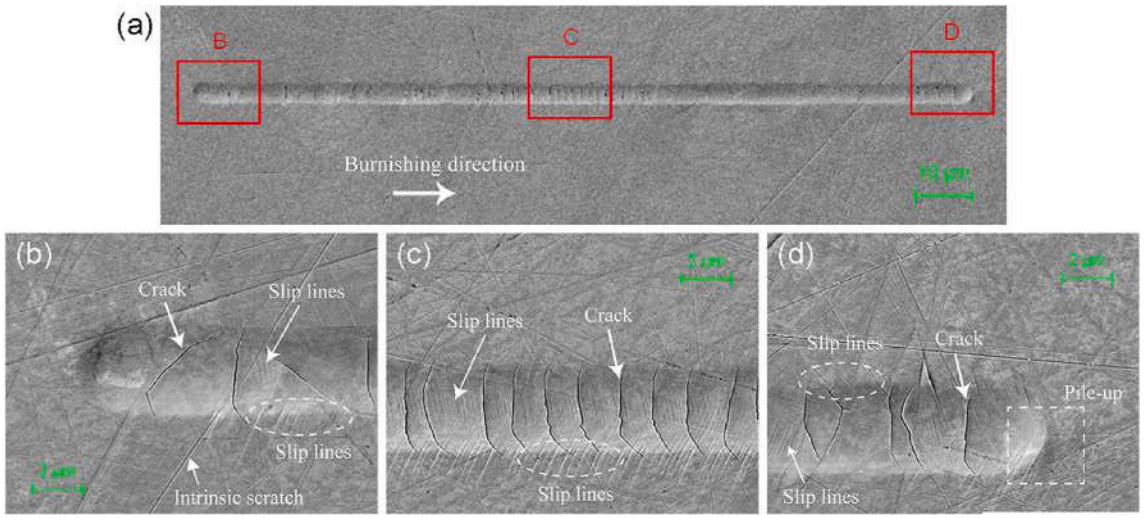

Fig. 5. SEM images of (a) burnished groove under the force of 10 mN with dry conditions; (b–d) corresponding close-up views of the regions, which were indicated by B, C, and D in (a).

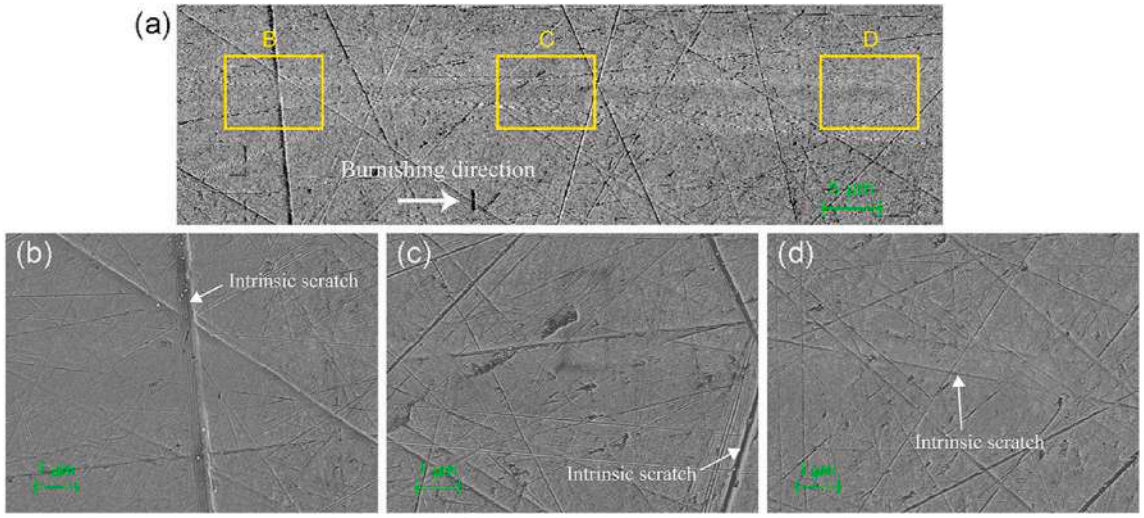

Fig. 6. SEM images of (a) burnished groove under a force of 2 mN with lubricated conditions; (b–d) corresponding close-up views of the regions, which were indicated by B, C, and D in (a).

deformed, owing to the sliding contact with the tool tip, which resulted in a reduction in surface roughness.

The groove burnished under lubricated conditions at 10 mN is shown in Fig. 8. It is evident from the close-up views that both cracks and slip lines formed in the burnished groove. However, in comparison with the burnished groove at the same force as that under dry conditions, the slip lines were less evident and could not be found at the groove edge. In addition, the pile-up at the end of the groove was not evident, as shown in Fig. 8(d). This confirms that the formation of slip lines at the groove edge was affected by the pile-up in front of the tool.

3.3. Effect of lubrication on deformation behaviour

Fig. 9 shows the penetration depth profiles of pre-scan, burnish, and post-scan grooves as functions of the burnishing distance under dry and lubricated conditions for the forces of 2 mN, 5 mN, and 10 mN. The burnishing profile and post-scan profile show gentle fluctuations. Because the workpiece is a polycrystalline material and the grains are randomly oriented, the mechanical properties change with grain orientation. In addition, small peaks (see arrows highlighted in Fig. 9) were observed in both the burnishing and post-scan profiles at the same location independent of the lubrication environment, indicating that the groove abruptly became shallower at these locations. The mechanism of this phenomenon is discussed in Section 3.4.

Fig. 10(a) shows effect of lubrication on average depths of burnished grooves. There is a general trend that the average depth of the surface profile obtained under lubricated conditions was smaller than that under dry conditions even under the same force, although this trend is not statistically significant because the surface profile varies violently with crystal grain orientations. The reason why the grooves formed under lubricated conditions were shallower might be that a small amount of oil was trapped in the interface and sandwiched between the tool and workpiece, although most of the oil was squeezed out during the burnishing process [26]. This viewpoint can be further confirmed by the fact that the difference in the average burnishing depths between dry and lubricated conditions became smaller when the force increased. However, the elastic recovery rate, that is, the ratio of the height of the elastic recovery to the penetration depth of the tool during the burnishing process, remained at the same level for different lubrication environments under the same force, as shown in Fig. 10(b). This means

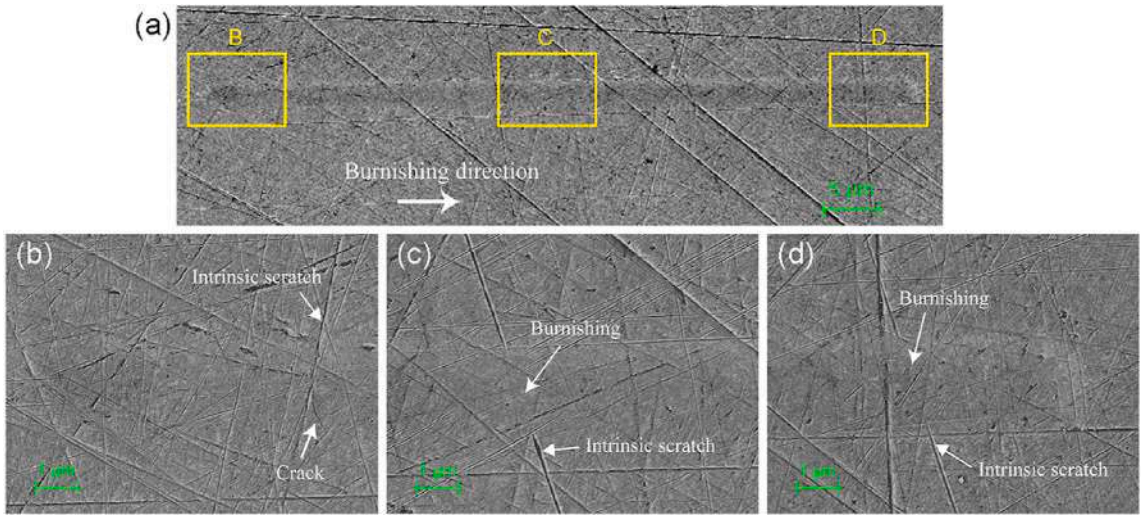

Fig. 7. SEM images of (a) burnished groove under a force of 5 mN with lubricated conditions; (b–d) corresponding close-up views of the regions, which were indicated by B, C, and D in (a).

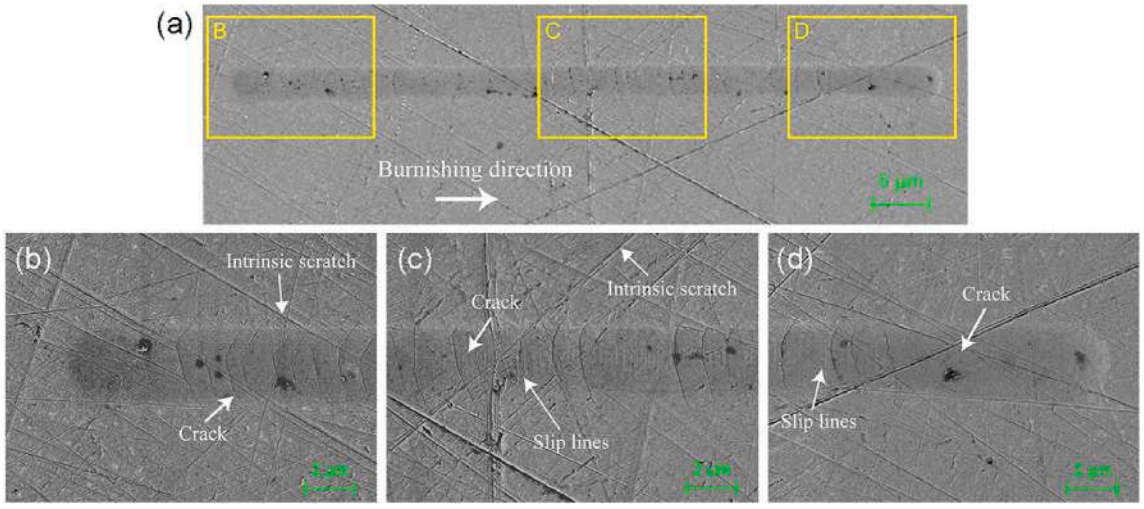

Fig. 8. SEM images of (a) burnished groove under a force of 10 mN with lubricated conditions; (b–d) corresponding close-up views of the regions, which were indicated by B, C, and D in (a).

that the introduction of lubricating oil did not lead to changes in the mechanical properties of the workpiece.

Fig. 11 shows the typical cross-sectional profiles of the grooves burnished under dry and lubricated conditions. As expected, under the same lubrication environment, the height of the pile-up increased as the force was increased. However, under the same force, the pile-up height under lubricated conditions was less than that under dry conditions even though the groove depth obtained with lubrication was greater. The formation of pile-up is a common phenomenon in the indentation of a material that exhibits a low strain-hardening potential [27]. When a normal force is applied, the material reveals a strong localization of the plastic deformation in the immediate vicinity of the tool tip, leading to a pile-up. In the burnishing process, however, the material is subjected to not only the pre-determined normal force but also to the tangential force induced by the sliding of the tool. Therefore, a pile-up would form in front of the tool. In Fig. 11, it is noteworthy that for all the cases, the pile-up was not completely symmetrical on both sides of the groove. The reason for this is that the activated slip plane is asymmetric with respect to the burnishing direction, which will be further discussed in Section 3.5.

Fig. 12 shows the AFM images of the end sections of the grooves burnished at 10 mN under dry and lubricated conditions, respectively. The detection errors in Fig. 12 (a) were caused by surface cracks at those locations. The profiles of the workpiece surface under both conditions (Dry-1 and Lubrication-1), which are in front of the exit point of the tool, are shown in Fig. 12(c). It is evident that the pile-up height under lubricated conditions was smaller than that under dry conditions, which is in conformity with the SEM observation (Figs. 5(d) and Fig. 8(d)). This indicates that the lubricating oil could reduce the material accumulation in front of the tool. This could be attributed to the reduced friction between the tool and workpiece due to oil lubrication at the interface. Consequently, at the side of the groove, the height of the pile-up under dry conditions (Dry-2) was larger than that under lubricated conditions (Lubrication-2), as shown in Fig. 12(c). The material accumulated in front of the tool was pushed aside as the tool moved forward.

3.4. *Effect of crystallographic orientations on surface generation*

In the ultraprecision turning of polycrystalline materials, such as copper [28] and germanium [29], it has been reported that a height difference appears at the grain boundary caused by the different crystal orientations of two adjacent grains, namely the grain boundary step,

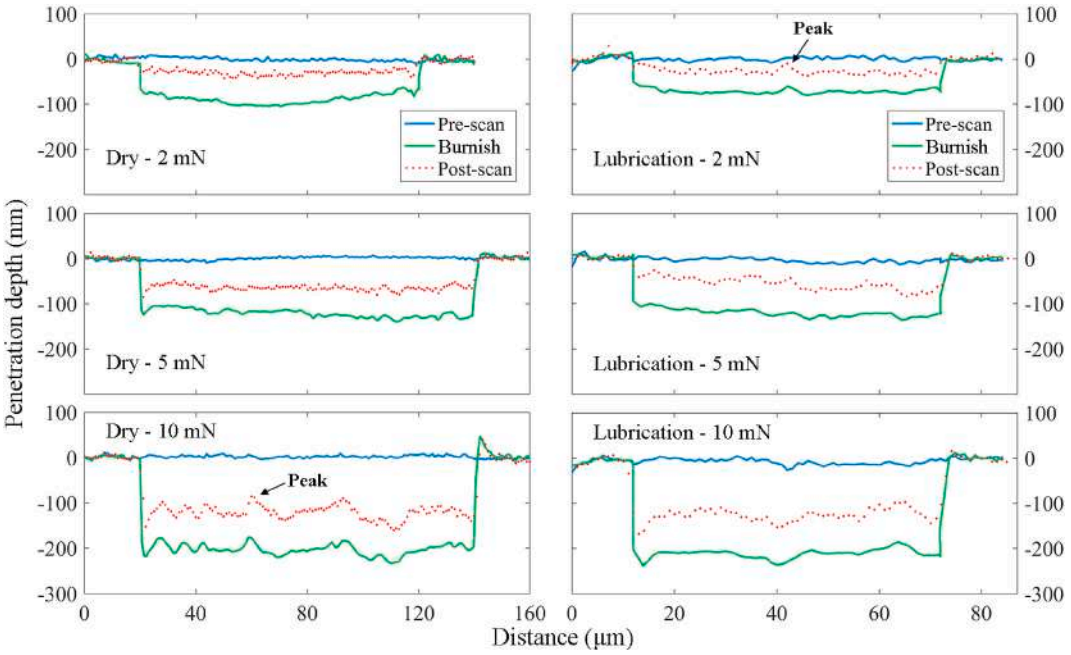

Fig. 9. Penetration depth of pre-scan, burnish, and post-scan as a function of the burnishing distance under dry and lubricated conditions for the forces of 2 mN, 5 mN, and 10 mN.

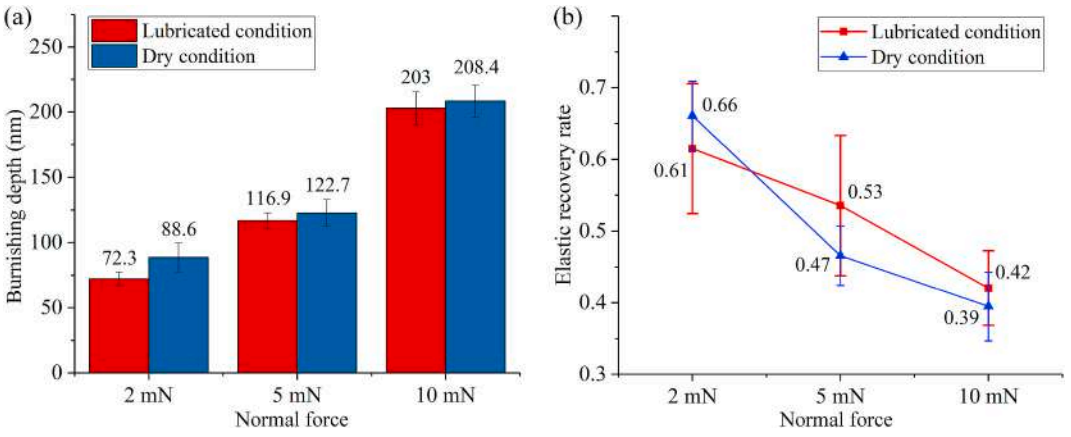

Fig. 10. Effects of lubrication on (a) average depth of the groove during burnishing process and (b) elastic recovery rate of the groove under different forces.

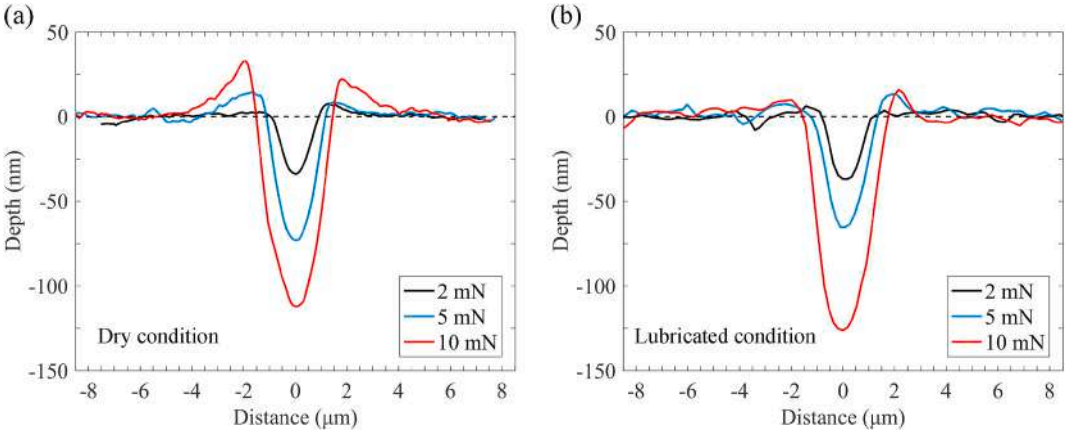

Fig. 11. Cross-section profiles of the burnished grooves under (a) dry and (b) lubricated conditions.

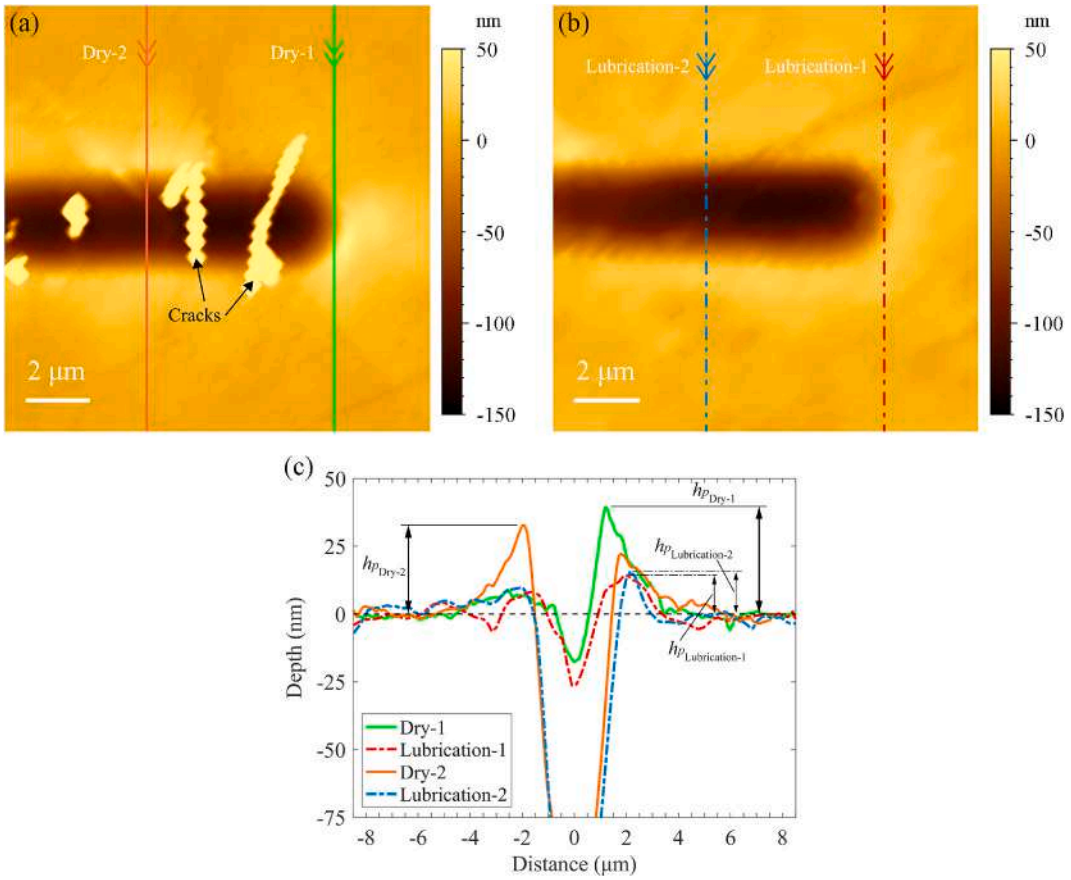

Fig. 12. AFM image of end part of the burnished groove conducted at the force of 10 mN under (a) dry conditions and (b) lubricated conditions. (c) Comparison of maximum height of pile-up (h_p) among corresponding cross-sectional profiles of the burnished grooves with dry and lubricated conditions.

which is the primary factor affecting surface roughness. The same phenomenon was observed in ultraprecision turning of *p*-ZnSe [30], although the grain boundary step was reduced to an acceptable level for optical applications. Hence, it is also important to investigate the formation of grain boundary steps in micro/nanoscale burnishing.

To clarify the effect of crystallographic orientations on the formation of surfaces, the distribution of the crystallographic orientations in the area of the burnished groove of 10 mN under dry conditions was characterised using EBSD. The crystal orientation mapping result for the area around the burnished groove was presented as the inverse pole figure (IPF) map shown in Fig. 13(a). Although there are noise points in the EBSD image due to the poor electrical conductivity of the sample, a typical area (outlined by a black box), which has two grains with different crystallographic orientations, could be extracted and analysed.

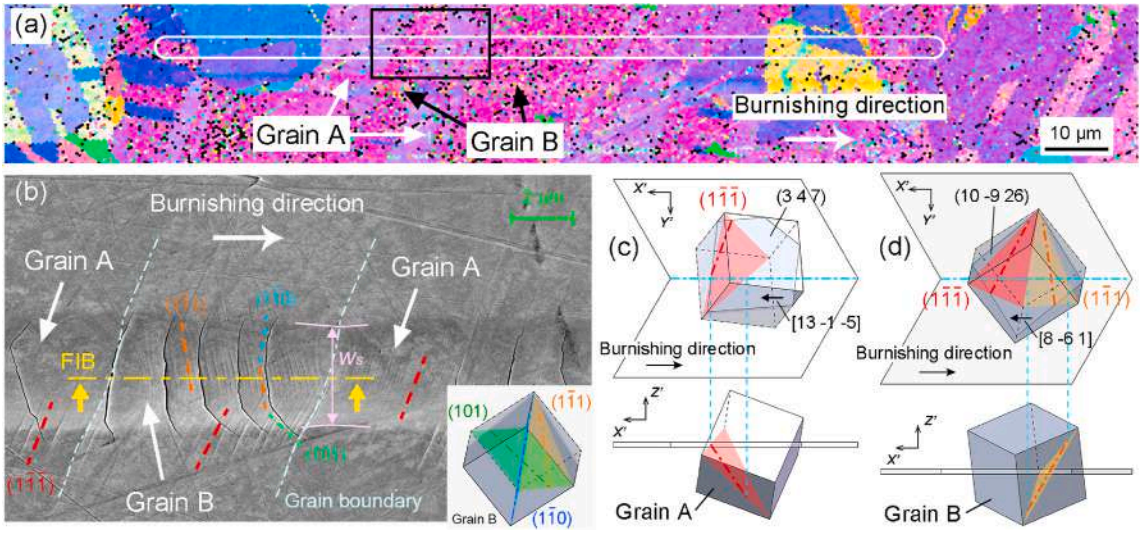

Fig. 13. (a) IPF map of the burnished groove under the force of 10 mN with dry conditions (the profile of the groove is represented by a solid white line); (b) corresponding SEM image of the region that is outlined by black box in IPF map (the bottom right inset sketches the cleavage plane and slip plane of grain B); (c) and (d) are schematic drawings of top and front views of the crystal orientation of grain A and grain B.

The SEM image of this area is shown in Fig. 13(b). The orientations of the two grains (Grains A and B) represented by Miller indices are (3 4 7) [13 -1 -5] and (10 -9 26) [8 -6 1], respectively. Fig. 13(c) and (d) show the orientations of these two grains from the top and side views. It is evident that, in Fig. 13(b), the location of the smallest groove width (w_s) corresponds to a grain boundary. In addition, in the penetration depth profile shown in Fig. 9, a peak feature should appear at this location, because the groove depth at this location has decreased. Thus, it can be inferred that in the penetration depth profile, each peak corresponds to a grain boundary.

To quantitatively evaluate the difference of the groove depth in the two neighbouring grains, the 3D surface morphology was measured by AFM, as shown in Fig. 14 (a). The cross-sectional profiles of the groove in grain A (blue line), grain B (red line), and grain boundary (black line) are plotted in Fig. 14 (b). It is observed that the groove depth in grain B is slightly larger than that in grain A, and the groove depth at the grain boundary is the smallest. In addition, the pile-up is mainly distributed on the right side of the groove in both grains A and B. This is because the material in front of the tool flowed more easily to the right side of the tool because of the specific activated slip planes in these two grains, as discussed in the next section.

3.5. Prediction of activated slip systems

The EBSD analysis revealed that the slip lines in grain A, at both the groove bottom and edge, were along the intersection vector between the slip plane (1 -1 -1) and workpiece surface plane, as shown in Fig. 13(c). In grain B, the slip line at the groove bottom was along the intersection vector between the surface plane and slip plane (1 -1 1), and the slip line at the groove edge was along that between the surface plane and slip plane (1 -1 -1), as shown in Fig. 13(d). The results indicate that in grain A, the slip plane (1 -1 -1) was activated, while in grain B, the slip planes (1 -1 1) and (1 -1 -1) were activated.

To predict the activated slip systems, a simplified Schmid's law-based model considering the relationship between the burnishing direction and crystal orientation was developed. According to the Schmid's law, the higher the Schmid factor, the more easily the slip system is activated [31]. During the burnishing process, the force acting on the workpiece can be decomposed in the direction normal to the surface ($\boldsymbol{n}$) and in the direction parallel to the surface ($\boldsymbol{V_i}$), as illustrated in Fig. 15. For the force parallel to the surface, the direction varies with the contact point between the tool and workpiece. As the slip line at the groove edge was caused by the pile-up being pushed aside by tool movement (see Fig. 5(d)), the force state of the pile-up was simplified to be subjected to an equivalent force at an angle of approximately 45° from the burnishing direction, as illustrated in Fig. 15, where $\boldsymbol{V_L}$ and $\boldsymbol{V_R}$ are force vectors. However, the slip line at the groove bottom was caused

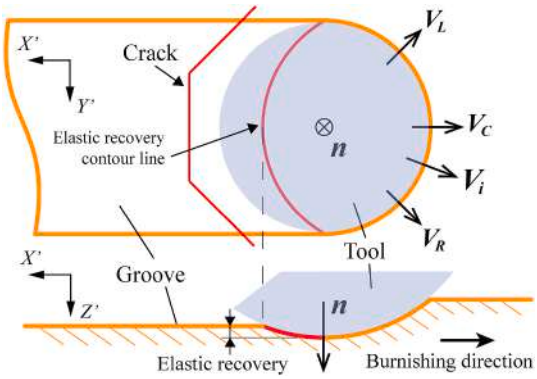

Fig. 15. Schematic of equivalent stresses acting on the workpiece during burnishing process.

by the material directly in front of the tool being pushed downwards. Thus, the force state of the material in front of the tool was simplified to be subjected to an equivalent force along the centre line, as indicated by $\boldsymbol{V_C}$ in Fig. 15. For the above force states, the effective Schmid factor can be obtained by superimposing the Schmid factors of the compression along the parallel direction of the surface and the compression along the normal direction of the surface. Consequently, the effective Schmid factor (m_s) can be expressed as [32].

$$m_s = \frac{\boldsymbol{V_i}\cdot\mathbf{SP}}{|\boldsymbol{V_i}|\cdot|\mathbf{SP}|}\times\frac{\boldsymbol{V_i}\cdot\mathbf{SD}}{|\boldsymbol{V_i}|\cdot|\mathbf{SD}|}-\frac{\boldsymbol{n}\cdot\mathbf{SP}}{|\boldsymbol{n}|\cdot|\mathbf{SP}|}\times\frac{\boldsymbol{n}\cdot\mathbf{SD}}{|\boldsymbol{n}|\cdot|\mathbf{SD}|} \tag{1}$$

where **SP** is the normal vector of the slip plane, and **SD** is the vector of the slip direction.

$$\boldsymbol{V_i} = \begin{cases} -[r\ s\ t]-[u\ v\ w] & i=L \\ -[u\ v\ w] & i=C \\ [r\ s\ t]-[u\ v\ w] & i=R \end{cases} \tag{2}$$

$$[r\ s\ t] = [h\ k\ l]\times[u\ v\ w] \tag{3}$$

Table 3 lists the Schmid factors of twelve possible slip systems in grains A and B, respectively. For grain A, it is predicted that the most favourable slip systems are (1 -1 -1) [1 1 0] at the groove centre with a Schmid factor of 0.79 and (1 -1 -1) [1 0 1] at the right edge of the groove with a Schmid factor of 0.88, respectively. In the experiment, the actual slip lines formed in grain A were observed at the groove centre and the right edge of the groove in directions parallel to the slip plane (1 -1 -1) of grain A, as shown in Fig. 13(b) and (c). Similarly, for grain B, it is predicted that the most favourable slip systems are (1 -1 1) [1 0 -1] at the groove centre with a Schmid factor of 0.85 and (1 -1 -1) [0 1 -1] at the

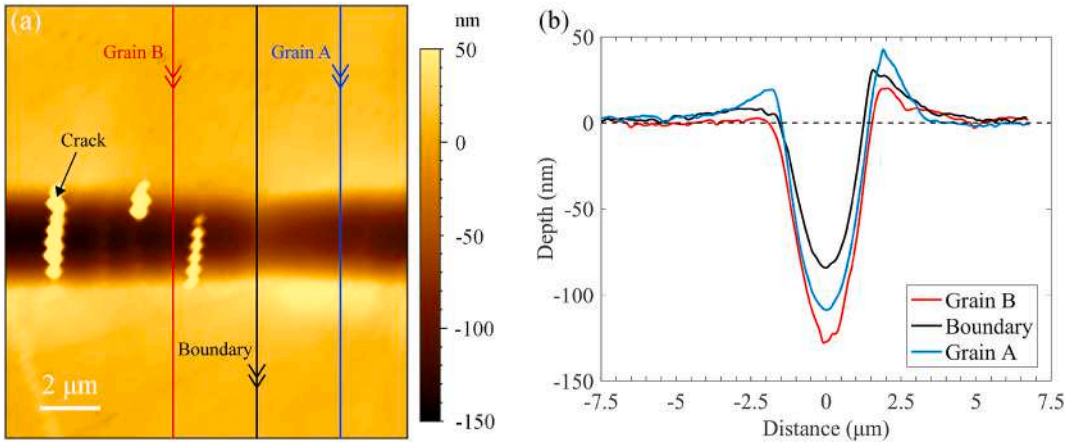

Fig. 14. (a) AFM image of the region indicated in Fig. 13(b). (b) Corresponding cross-sectional profiles of the burnished groove.

Table 3
Calculated Schmid factors of the twelve slip systems in grains A and B. Schmid factors of the predicted activated slip system are bolded for each grain.

Slip system		Schmid factor (grain A)			Schmid factor (grain B)		
Plane	Direction	V_L	V_C	V_R	V_L	V_C	V_R
(1 1 1)	[1 $\bar{1}$ 0]	0.08	0.28	0.15	0.47	0.17	−0.46
	[1 0 $\bar{1}$]	0.58	0.57	0.34	0.42	0.20	−0.06
	[0 1 $\bar{1}$]	0.50	0.29	0.19	−0.05	0.03	0.40
(1 1 $\bar{1}$)	[1 $\bar{1}$ 0]	0.01	0.50	−0.01	0.19	0.04	−0.25
	[1 0 1]	0.00	0.28	0.00	0.68	0.38	0.35
	[0 1 1]	0.00	−0.21	0.00	0.49	0.34	0.60
(1 $\bar{1}$ 1)	[1 1 0]	−0.50	−0.01	−0.20	0.73	0.35	−0.05
	[1 0 $\bar{1}$]	−0.14	0.47	0.53	0.69	**0.85**[c]	0.60
	[0 1 1]	−0.36	−0.48	−0.73	0.04	−0.51	−0.65
(1 $\bar{1}$ $\bar{1}$)	[1 1 0]	0.58	**0.79**[a]	0.34	−0.07	−0.14	−0.67
	[1 0 1]	0.44	0.76	**0.88**[b]	0.43	0.68	0.18
	[0 1 $\bar{1}$]	0.14	0.03	−0.54	−0.50	−0.82	**−0.85**[d]

[a] Slip system (1 -1 -1) [1 1 0] activated at the groove centre in grain A (see Fig. 13 (b) and (c)).
[b] Slip system (1 -1 -1) [1 0 1] activated at the right edge of the groove in grain A (see Fig. 13 (b) and (c)).
[c] Slip system (1 -1 1) [1 0 -1] activated at the groove centre in grain B (see Fig. 13 (b) and (d)).
[d] Slip system (1 -1 -1) [0 1 -1] activated at the right edge of the groove in grain B (see Fig. 13 (b) and (d)).

right edge of the groove with a Schmid factor of −0.85, respectively. The actual slip lines formed in grain B were observed at the groove centre and the right edge of the groove in directions parallel to the slip plane (1 -1 1) and (1 -1 -1) of grain B, respectively, as shown in Fig. 13(b) and (d). These results reveal that the theoretically predicted active slip systems are consistent with the experimental observations for both grains A and B, which strongly validates the simplified Schmid's law-based model developed in this study.

3.6. Crack formation mechanism

As observed in Fig. 13(b), crack deflection occurred in grain B. Considering the EBSD analysis, as shown in the inset of Fig. 13(b), it is revealed that the crack at the groove bottom propagated along the intersection vector of the workpiece surface plane with the slip plane (1 -1 1). In contrast, the cracks near the right and left groove edges were propagated along the intersection vector of the workpiece surface plane with the (1 0 1) and (1 -1 0) cleavage planes, respectively. Thus, it can be inferred that the crack at the groove bottom was propagated along the slip plane, and the crack at the groove edge propagated along the cleavage plane.

To verify this inference, it is necessary to consider the experimental results in conjunction with the existing analytical models. Previous studies have reported that the stress field responsible for brittle fracture can be developed by combining the point normal force (F_N)-induced Boussinesq field and the tangential force (F_T)-induced Cerruti field as well as the Blister field, owing to the residual stress, which is contributed by the local inelastic deformation surrounding the groove [25,33,34]. Thus, the normal and shear stresses are given by

$$\sigma = \sigma^{n}_{\text{Boussi.}} + \sigma^{t}_{\text{Cerruti}} + \sigma^{r}_{\text{Blister}} \tag{4}$$

$$\tau = \tau^{n}_{\text{Boussi.}} + \tau^{t}_{\text{Cerruti}} + \tau^{r}_{\text{Blister}} \tag{5}$$

The relevant coordinate system is shown in Fig. 16, where a_c is the contact area radius of the groove, and is approximately equal to the radius of the surrounding semi-cylindrical inelastic zone [35]. The detailed equations for modelling each stress field are given in the appendix of this paper.

It has been widely accepted that two main factors contribute to forces in burnishing: the ploughing force (F_p) caused by the workpiece deformation, and the interface friction force (F_f) between the tool and workpiece [36]. Thus, as shown in Fig. 16, the normal force (F_N) and tangential force (F_T) can be estimated by

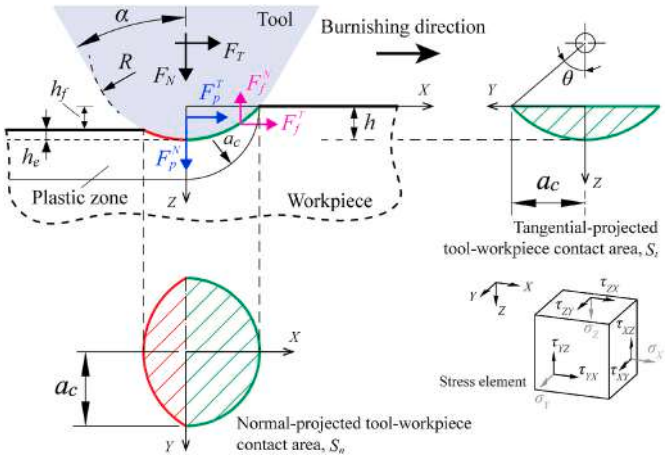

Fig. 16. Schematic of the burnishing process and contact area for the conical tool, as well as the coordinate system of the burnished groove for the stress field calculation.

$$F_N = F_p^N + F_f^N \tag{6}$$

$$F_T = F_p^T + F_f^T \tag{7}$$

To estimate F_T, two assumptions were made in advance: (1) F_f^N is negligibly small in comparison with the predetermined normal force owing to the extremely small penetration depth; (2) the mean contact pressure (P_{mean}) caused by the ploughing force along the normal and tangential directions are the same. That is, $F_p^N = P_{mean} \cdot S_n$ and $F_p^T = P_{mean} \cdot S_t$ [37]. Consequently, F_T can be rewritten as

$$F_T = \frac{S_t}{S_n} F_N + \mu F_N \tag{8}$$

where S_t/S_n is the ploughing friction coefficient [37] and μ is the coefficient of interface friction between the tool and the workpiece. The value of F_N is equal to the predetermined normal force applied in the burnishing test. S_n and S_t are normal-projected tool-workpiece contact area and tangential-projected tool-workpiece contact area, respectively, which are given by Ref. [38]:

$$S_n = \frac{1}{2}\pi\left(2Rh - h^2\right) + \frac{4}{3}\sqrt{2Rh - h^2} \times\sqrt{2\left(R + h_f\right)h - \left(2Rh_f + h_f^2 + h^2\right)} \tag{9}$$

$$S_t = R^2 \arccos\left(\frac{R-h}{R}\right) - (R-h)\sqrt{h(2R-h)} \tag{10}$$

In the burnishing test, the value of the interface friction coefficient under lubricated condition should be smaller than that under dry conditions. Therefore, two interface friction coefficients, 0.1 (lubricated condition) and 0.4 (dry condition), respectively, were chosen for plotting the stress distribution along the burnishing direction. By substituting F_N and F_T in each stress field model (see Appendix A), the distribution of normal stress σ_X along the X direction and the distribution of shear stress τ_{XZ} along the X direction in the vicinity of the tool tip can be plotted.

Fig. 17 illustrates the stress distribution in the XZ plane at $Y = 0$ under $F_N = 5$ mN. It is observed that in the area below the tool, normal stress and shear stress were less affected by the interfacial friction coefficient. The normal stress σ_X at the rear of the tool is tensile stress, which increases with the friction coefficient. The shear stress τ_{XZ} at the front and rear of the tool also increases with the friction coefficient. It must be noted, however, that in the estimation of the tangential force the effect of pile-up was ignored, as a result, the value of tangential force used in the model was smaller than the actual value. Especially for the dry condition, the actual tangential force should be much larger than the estimated one, because larger pile-ups formed under the dry condition (see Fig. 12). Therefore, the actual difference of stresses between dry and lubricated conditions should be more significant than that indicated by the curves plotted in Fig. 17. That is, the tensile tress at the rear of the tool and the shear stress at the front and rear of the tool under the dry conditions are much larger than those under the lubricated conditions. Moreover, as the stress with the maximum value is the tensile stress at the rear of the tool, it should be responsible for crack nucleation in a brittle material [39]. This may explain the reasons why the cracks in the groove of 5 mN were not along the slip lines, and why cracks were generated more significantly at the dry condition (see Fig. 4) than that at the lubricated condition (see Fig. 7).

To demonstrate the difference in stress distribution in the groove bottom and edge, the distribution of normal stress and shear stress in the XZ plane at $Y = 0$ (groove bottom) and $Y = 0.6a_c$ (groove edge) under $F_N = 10$ mN are plotted in Fig. 18. It is observed that, at the groove edge, the tensile stress is dominant at the rear of the tool. At the groove bottom, the tensile stress is also dominant at the rear of the tool, but the shear stress is dominant below the tool. Therefore, it can be inferred that the crack deflection is caused by the competition of the stress fields: (1) the tensile stress is dominant behind the tool at the groove edge, which results in crack propagation along the cleavage planes; (2) the combined effect of tensile stress and shear stress at the groove bottom leads to crack propagation along the slip planes. As discussed in Fig. 5, the cracks were caused by material elastic recovery after the tool had passed through. Owing to the geometric feature of the conical tool, the contour line of the elastic recovery was an arc, as shown in Fig. 15. Thus, the slip plane and cleavage plane that intersect with the workpiece surface plane to form a line, which is approximately tangent to the contour line, are more likely to fracture, causing the crack pattern to resemble an arc that is concave in the direction of burnishing (see Fig. 13(b)).

Fig. 19 shows a schematic diagram of the defect evolution during the burnishing process. The defect of slip lines appears first in the tool-workpiece contact area caused by the sliding of the tool, while at the same time the pile-up forms in front of the tool, as illustrated in Fig. 19 (a). As the tool continues to slide forward, more pile-up is accumulated and pushed to the side, accompanied by the propagation of slip lines from the pile-up, as illustrated in Fig. 19(b). Meanwhile, the material below the tool undergoes an elastic recovery, which may result in crack propagation along the slip plane at the groove bottom due to the combined effect of shear stress and tensile stress, and in crack propagation along the cleavage plane at the groove edge due to tensile stress, as illustrated in Fig. 19(c).

3.7. Subsurface microstructural changes

To evaluate the burnish-induced changes in the crystal structure, Raman line-mapping was conducted in a groove burnished at 10 mN under dry conditions. The scanning path was perpendicular to the burnishing direction and the groove centreline was taken as the axis of symmetry. The length of the scanning path was 8 μm, with a pitch of 0.2 μm. Fig. 20 shows the 3D plot of Raman shift vs. Y position vs. Raman intensity. Three peaks at approximately 140.5, 206.2, and 253.1 cm^{-1} were clearly observed, which correspond to the transversal acoustic (2 TA), transversal optical (TO), and longitudinal optical (LO) phonon modes of ZnSe, respectively [30]. No phase transformation was observed in the burnished groove. However, the Raman peak weakening for 2 TA, TO, and LO was observed at the groove centre. This is assumed to be caused by local lattice distortion in the material subsurface [40]. As no material was removed from the workpiece surface and the material underwent plastic ploughing during the burnishing process, the material at the groove centre underwent additional compression and shear, resulting in more severe local lattice distortion with less Raman intensity. This is proven by the LO peak of the Raman spectrum (inset, Fig. 20). At the groove centre, the LO peak shifted to a higher value, indicating greater compressive residual stress caused by the burnishing process. The phenomenon that volume compression of the material is accompanied by lattice distortion without the observation of phase transformation might be attributed to the fact that the phase

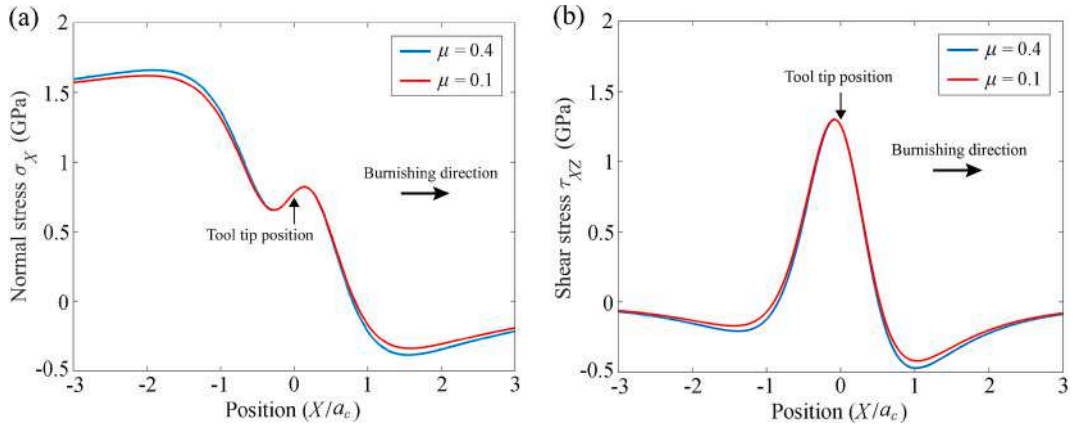

Fig. 17. Distribution of (a) normal stress σ_X and (b) shear stress τ_{XZ} along the X direction in the XZ plane at $Y = 0$, under $F_N = 5$ mN.

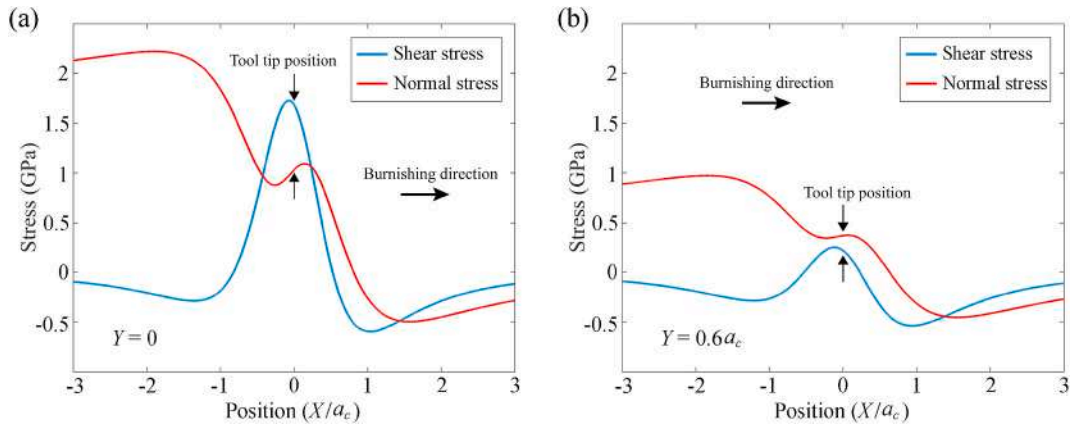

Fig. 18. Distribution of normal stress σ_X and shear stress τ_{XZ} along the X direction in the XZ plane at (a) $Y = 0$ and (b) $Y = 0.6a_c$, under $\mu = 0.4$ and $F_N = 10$ mN.

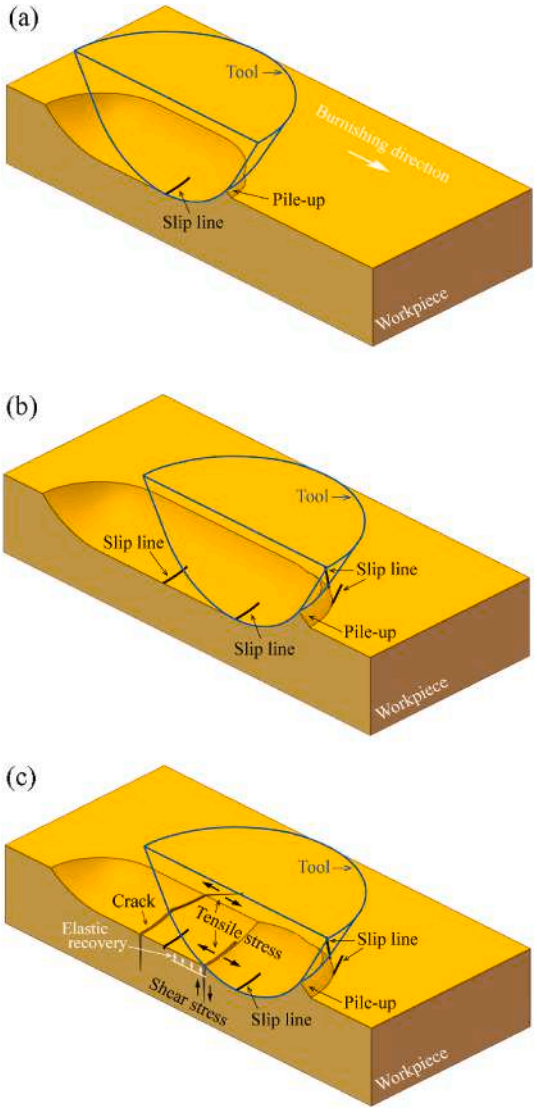

Fig. 19. Schematic diagram of the defect evolution during the burnishing process: (a) formation of the slip line at the groove bottom; (b) formation of the slip line at the groove edge; (c) generation of the crack in the groove after elastic recovery.

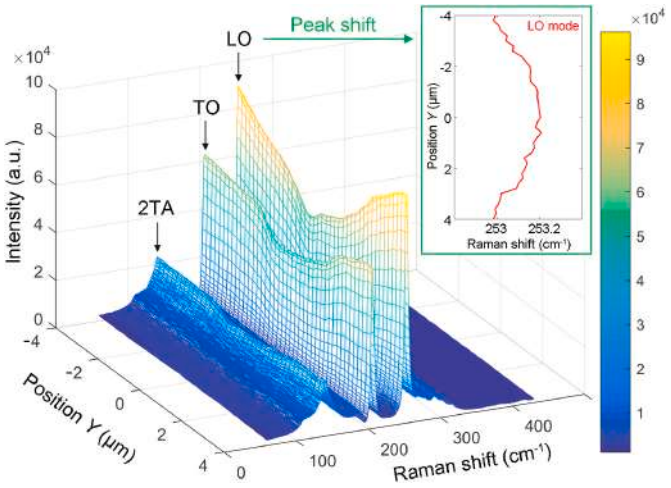

Fig. 20. Raman line mapping spectra acquired from positions along the line which is perpendicular to the burnishing direction for the burnished groove under the force of 10 mN with dry conditions (The inset presents the Raman peak shift of LO mode).

transformation of ZnSe caused by the compressive hydrostatic stress is completely reversible during unloading [23]. However, the lattice distortion could be held by the compressive residual stress, and as a result, the lattice distortion could not be completely recovered after unloading. This phenomenon has also been reported in nanoscratching of GaAs [41], which has physical properties similar to those of ZnSe. For optical and optoelectronic applications, lattice distortion in the subsurface region may affect the optical and electrical properties of the surface. For example, in polycrystalline In_2O_3:Sn (ITO) films, the electron density decreases linearly with the increase in lattice distortion, and consequently the refractive index increases [42]. The effect of lattice distortion on surface properties will be further investigated in the future.

To further understand the deformation behaviour of the subsurface layer of the burnished groove, a cross-section of the groove was prepared by FIB milling along the burnishing direction at the groove bottom, as indicated in Fig. 13(b). Fig. 21(a) shows a TEM image of the corresponding cross-sectional area. It is observed that the region underneath the burnished groove was severely deformed with dislocations in parallel macroscopic bands, which were oriented along the activated slip planes of grains A and B, respectively (Fig. 13(c) and (d)). To investigate the microstructural characteristics of the material at different depths after burnishing, the selected area electron diffraction (SAED) patterns at the top surface and 850 nm below the surface in both grains A and B are presented in Fig. 21(a): A1, A2, and B1, B2, respectively. It is noticed

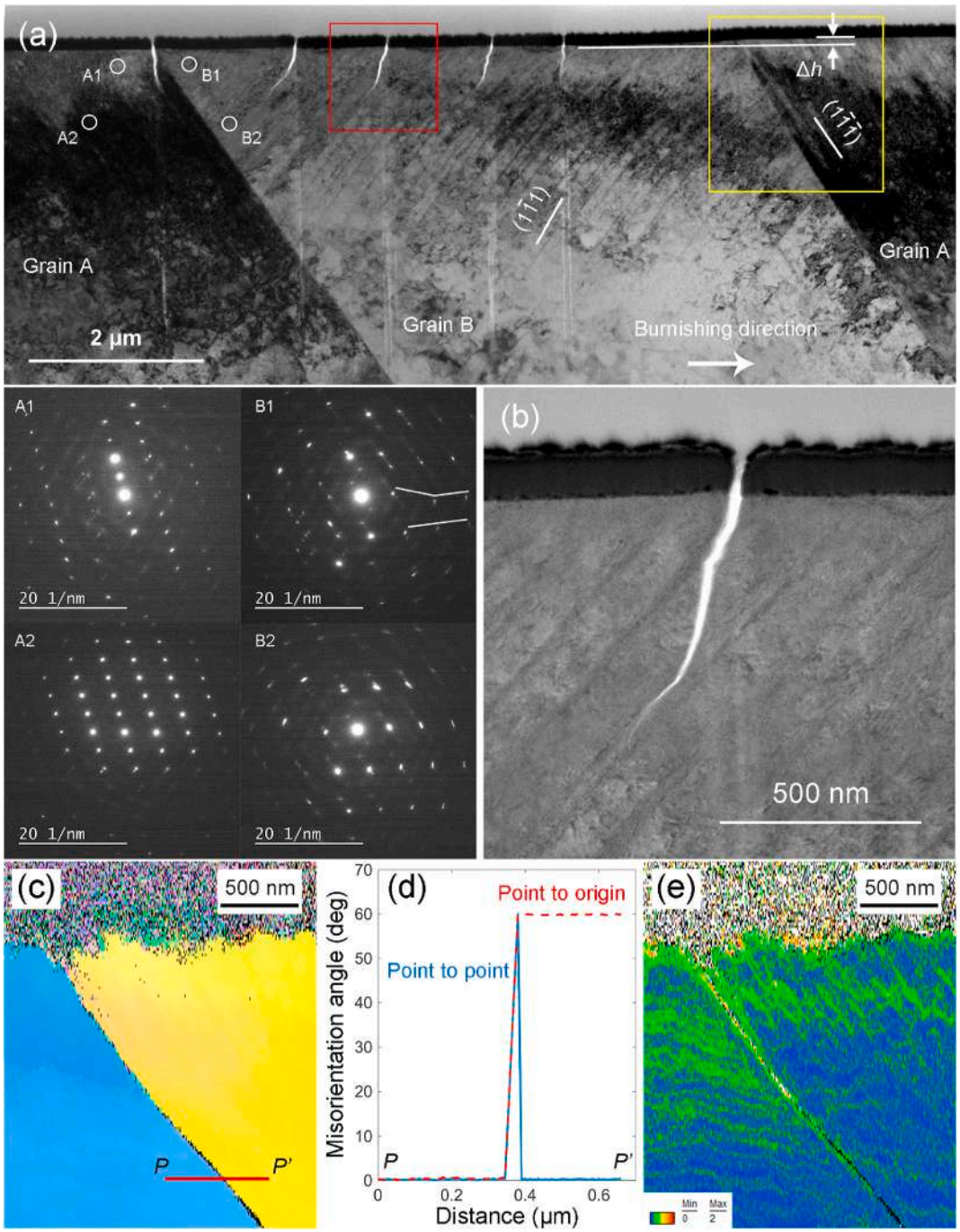

Fig. 21. (a) An overall cross-sectional TEM image of the region indicated in Fig. 12(b); Figs. A1, 2 and B1, 2 are SAED patterns of corresponding areas circled in (a). (b) Close-up view of the region outlined by red box in (a). (c) IPF map of the region outlined by yellow box in (a). (d) Misorientation angle profile along Line *PP*′ marked in (c). (e) KAM map of the region outlined by yellow box in (a). (For interpretation of the references to colour in this figure legend, the reader is referred to the Web version of this article.)

that in grain A, the diffraction spot shape at 850 nm below the surface (Fig. 21(a), A2) was round but changed to an ellipse at the top surface (Fig. 21(a), A1). This indicates that lattice distortion occurred within the shallow subsurface of grain A [41]. In contrast, in grain B, the SAED patterns at both the top surface (Fig. 21(a), B1) and 850 nm below the surface (Fig. 21(a), B2) presented an elliptical spot shape, indicating that the lattice distortion in grain B was more extensive. In addition, the SAED pattern at the top surface (Fig. 21(a), B1) shows that the spots were not aligned parallel to one common direction, indicating a more severe lattice distortion that occurred within the shallow subsurface of grain B. It can also be seen from Fig. 21(a) that at the grain boundary on the left of the figure, a crack was generated, and at the grain boundary on the right of the figure, a notable height difference between the surface of grains A and B was generated, which is consistent with the result in Fig. 13(b). By observing the image of the subsurface of grain B with a higher magnification, as shown in Fig. 21(b), it can be seen that the crack propagation is not only along the direction parallel to the slip band, but also tends to deflect in the direction perpendicular to the burnishing direction. These results support the viewpoint that the combined effect of shear stress and tensile stress caused the crack to grow. Cross-sectional analysis with EBSD provides further support for understanding subsurface deformation behaviour. Fig. 21(c) shows the

IPF map of the vicinity of the grain boundary, which is outlined by the yellow box in Fig. 21(a). It can be seen that no grain refinement occurred, although there were large numbers of dislocations in the subsurface layer. This phenomenon is different from that observed in single-crystal KDP [2] and polycrystalline zirconia [43], in which fine grains are generated owing to the evolution of dislocations. The misorientation angle between grains A and B along Line *PP'* was extracted from the IPF map, as plotted in Fig. 21(d). This shows that the misorientation angle between the two grains is 60°, which indicates that grains A and B are twin pairs having a coherent twin boundary around <111> [30]. Fig. 21(e) shows the kernel average misorientation (KAM) map of the same region as that in Fig. 21(c). KAM quantifies the average value of the misorientations of a point with respect to all its neighbouring points [44]. In this mode, generally, it can reveal the geometrically necessary dislocation density and residual strain level in the material. For high KAM in deformed grains, a high plastic strain is expected [45]. Therefore, it is obvious that grain B underwent a larger plastic deformation than grain A, and the twin boundary could block the dislocations spreading into the adjoining twin.

3.8. Surface patterning

In diamond turning, material removal (chip formation) results in an extremely small undeformed chip (~20 nm) [30]. However, this study shows that in burnishing, material removal does not occur even when the penetration depth is more than 208 nm. This might be due to the different shapes of the tools used, which directly affect the relative tool sharpness (*RTS*), that is, the ratio of penetration depth (undeformed chip thickness for turning) to tool edge radius. Because the cutting-edge radius of the tool for turning is approximately 50 nm [30], and the radius of the tool tip for burnishing is 10 μm, the *RTS* of turning and burnishing are 0.4 and 0.0208, respectively. The extremely small *RTS* of burnishing compared with the *RTS* of turning will cause a much higher effective negative rake angle. The intense compressive stress imposed by the rounded edge curvature transforms a concentrated shear deformation mechanism into a rubbing mechanism [46].

Although no material removal occurs under a large penetration depth with a blunt tool, the aforementioned results indicate that cracks start to generate in the burnished groove when the normal force reaches 5 mN, corresponding to a groove depth of ~70 nm (Note that the critical force and groove depth are dependent on workpiece material properties and tool radius). Thus, applying a force smaller than this critical value may enable the fabrication of microstructures in ductile mode. Next, the feasibility of fabricating surface patterns by burnishing in a ductile mode was verified by creating grid microstructures on the *p*-ZnSe surface.

Fig. 22(a) shows the 3D topography of a groove-crossing grid microstructure with a pitch of 10 μm, which was fabricated with a force of 2 mN under dry conditions. The cross-sectional profiles along the diagonal and horizontal directions are presented in Fig. 22(b) and (c), respectively. The pattern was generated in a ductile mode without visible surface defects. In addition, it is evident that the depth of the groove at the intersecting area is larger than that of other areas. This is because burnishing was performed under the force-control mode, and multiple tool passes caused deeper tool penetration into the workpiece material. It is noted, however, that the depth of the intersecting area of the cross-burnished groove is less than twice the depth of a single burnished groove. This may be due to the fact that the strain hardening of material after the first burnishing reduced the burnishing depth for the second tool pass.

The SEM image of the groove-crossing grid microstructure is presented in Fig. 22(d). A part of the region (outlined by the white box in Fig. 22(d)) was extracted by AFM to characterise the surface roughness,

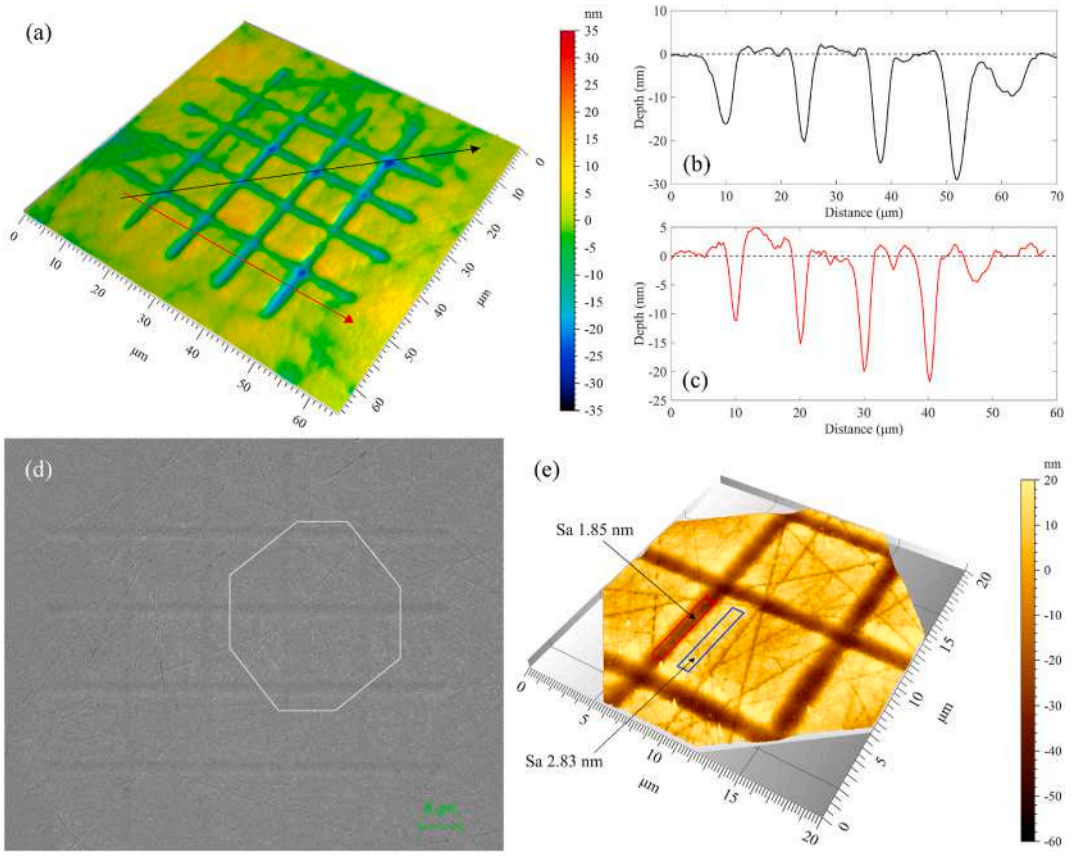

Fig. 22. (a) 3D topography of groove-crossing grid microstructure; (b) cross-sectional profile along the diagonal direction; (c) cross-sectional profile along the horizontal direction; (d) SEM image of groove-crossing grid microstructure; (e) AFM measurement of the region marked in (d).

as shown in Fig. 22(e). The mean surface roughness within an area of $0.6 \times 6\ \mu m^2$ in the burnished groove was 1.85 nm Sa, less than that of the polished workpiece surface (2.83 nm Sa). This demonstrates that burnishing is beneficial for the reduction of surface roughness. The burnished surface roughness is comparable to, or even better than, that of the diamond-turned surfaces of *p*-ZnSe reported in previous studies [30,47].

Another grid microstructure was fabricated by conducting an overlapped feed movement of the tool under a force of 2 mN under dry conditions. Three different feed pitches (*f*), that is, the distance between two neighbouring burnishing paths, were set as $f = 0.5$, 1, and 1.5 μm for fabricating different grid areas. During the processing of each grid, the burnishing paths were divided into two groups, where the paths of the same group were 2*f* apart from each other, as shown in the inset in Fig. 23(a). The size of each grid area was $10 \times 10\ \mu m^2$. Fig. 23(a) shows the 3D topography of the groove-overlapping grid microstructure. The cross-sectional profile of the grids along the feed direction is shown in Fig. 23(b). It was observed that the maximum waviness height of the grid surface was more than 10 nm. This might be caused by the crystallographic effect of the grains in the material.

The SEM image of the groove-overlapping grid microstructure is presented in Fig. 23(c). No cracks were found on the burnished surface. The intrinsic scratches of the workpiece surface inside the grid were not as obvious as those outside the grid. Three grids of different feed pitches (indicated in Fig. 23(c)) were extracted by AFM measurement to characterise the surface roughness, as presented in Fig. 23(d)–(f). The mean surface roughness of the grids at feed pitches of 0.5, 1, and 1.5 μm were 4.5, 7.3, and 8.3 nm Sa, respectively, within an area of $7 \times 7\ \mu m^2$. As shown in Fig. 23, the grid was formed through the overlapped grooves. Thus, the surface integrity of the grid deteriorated with increasing feed pitch. For all the aforementioned surface patterning tests, no chip formation was found by observing the tool tip and burnished surfaces after burnishing.

Fabricating such micropatterns on optical materials has received great interest in recent years due to its superiority in optical performance and/or structure optimisation, such as enhancement of sensitivity, increase of field of view, and miniaturisation of components [48]. These grid structures can also be used as micro/nanoscale fluidics, which are widely used in biomedical analysis. It should be pointed out that in this study, the burnishing tests were performed in a force-control mode using indentation/scratching equipment, where high form accuracy is difficult to achieve. Such burnishing tests can also be performed in a depth-control mode using an ultraprecision machine tool instead of a nanoscratching system. In such a case, the burnishing depth change due to multiple tool passes will be minimised. Consequently, form accuracy at a single nanometre level is achievable.

4. Conclusions

Micro/nanoscale burnishing tests were conducted on *p*-ZnSe, and the local plastic deformation behaviours as well as subsurface damage formation mechanisms were investigated to explore the possibility of chip-free surface patterning. The effect of lubrication was also characterised. The main conclusions are summarised as follows:

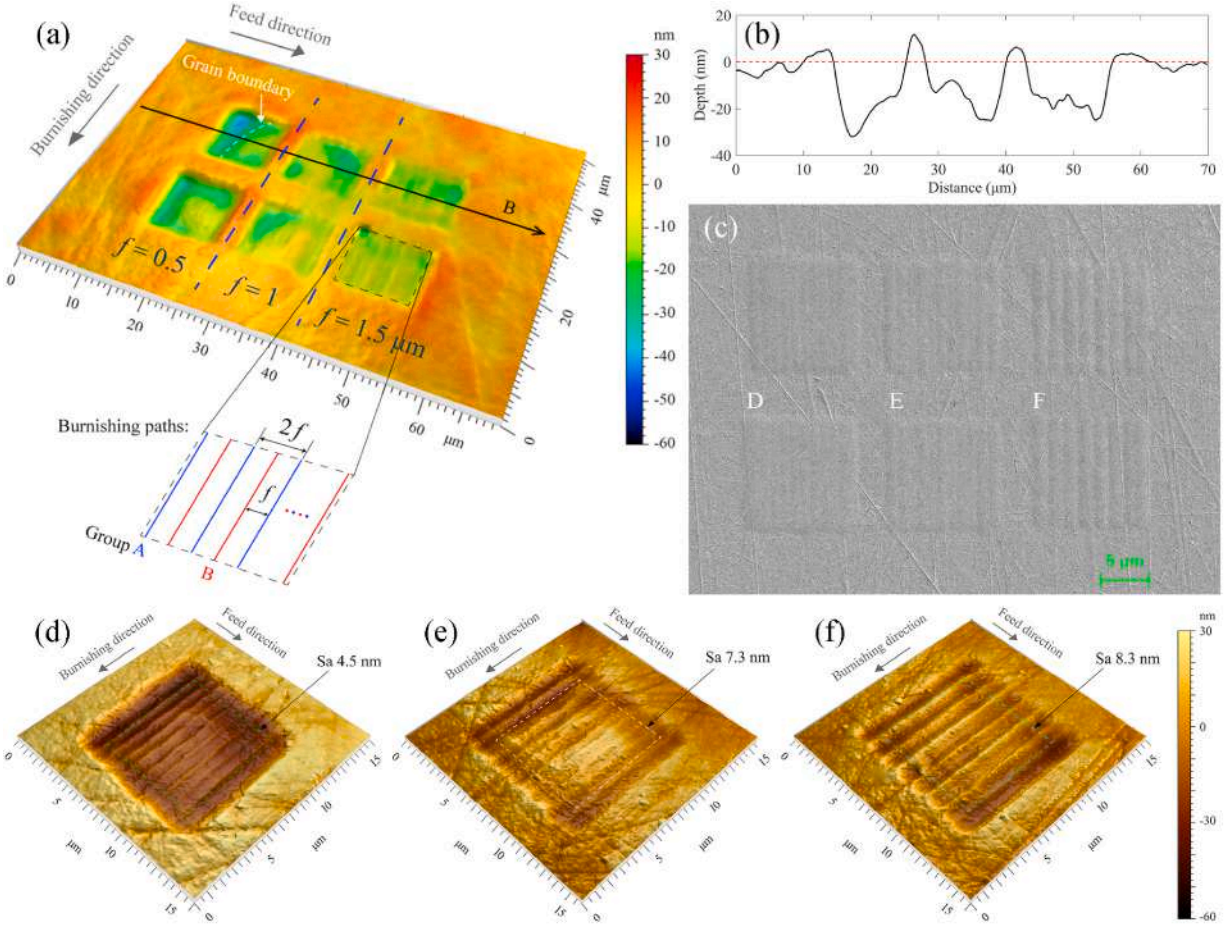

Fig. 23. (a) 3D topography of groove-overlapping grid microstructure; (b) cross-sectional profile along line B, as marked in (a); (c) SEM image of groove-overlapping grid microstructure; AFM measurement of the grids, as indicated by D, E and F in (c), which were fabricated under (d) $f = 0.5$ μm, (e) $f = 1$ μm, (f) $f = 1.5$ μm, respectively.

(1) Despite the high brittleness, *p*-ZnSe underwent local plastic deformation during burnishing. The surface roughness was reduced to the nanometric level, and compressive residual stress was enhanced. The depth of the burnished groove under lubricated conditions was smaller than that under dry conditions. The lubricating oil could reduce the material accumulation in front of the tool.
(2) Slip lines are formed in the region where the tool contacts the workpiece and in front of a pile-up around the tool. The slip lines are caused by the sliding of the material along the slip planes. The developed model for calculating the maximum Schmid factor of slip systems can predict the activated slip planes.
(3) Two types of cracks were observed at a force higher than the critical value. One propagates along the slip planes at the groove bottom caused by the elastic recovery of the material after the tool passes. The other propagates along the cleavage planes near the groove edge. The generation of cracks occurs after the formation of slip lines.
(4) No phase transformation was observed in the burnished groove. Instead, local lattice distortion appeared in the subsurface layer as a result of plastic deformation. The level of lattice distortion is gradually reduced from the groove centre to the groove edge.
(5) The resistance to dislocation motion varies with grain orientation. The twin boundary blocks the dislocations spreading into the adjoining twins; hence, a height difference occurs at the twin boundary. Strain hardening occurred in the surface layer of the burnished groove; thus, the depth of the second tool pass became smaller than that of the first one.
(6) Groove-crossing grid and groove-overlapping grid microstructures were fabricated on the *p*-ZnSe surface with surface roughness of 1.85 nm Sa and 4.5 nm Sa, respectively, by burnishing in a ductile mode without chip generation.

The results of this study demonstrate that burnishing is an effective method for producing micro/nanoscale surface structures on brittle polycrystalline materials in ductile mode. As no chip is generated in this process, the method is especially useful for preventing debris pollution in microfabrication of toxic materials. The findings from this study provide a reference for the clean production of ultra-precision surface patterns for optical applications and related areas. As the critical force and depth for crack-free burnishing are dependent on workpiece material property and tool shape, more quantitative experiments are required in the future to establish a series of guidelines for the production process. In addition, a comprehensive analytical model that correlates the critical force and depth of burnishing with material properties and tool shapes for burnishing polycrystalline soft-brittle material will be developed.

Author statement

Weihai Huang: Data curation, Investigation, Writing – original draft. Jiwang Yan: Conceptualization, Methodology, Supervision, Writing-Reviewing and Editing.

Declaration of competing interest

The authors declare that they have no known competing financial interests or personal relationships that could have appeared to influence the work reported in this paper.

Acknowledgements

This work has been partially supported by KLL Ph.D. Program Research Grant of Keio University. Thanks are extended to Mr. Tomoyuki Takano, Mrs. Sachiko Kamiyama, Mrs. Satomi Kojima and Mrs. Ayuko Kawakami in the Central Testing Center of Keio University for their technical assistance in SEM, EBSD and TEM observations as well as sample preparation.

Appendix A

The point normal force (F_N)-induced Boussinesq field is as follows:

$$\sigma_x^n = \frac{F_N}{2\pi}\left\{\frac{1-2\nu}{r^2}\left[\left(1-\frac{z}{\rho}\right)\frac{x^2-y^2}{r^2}+\frac{zy^2}{\rho^3}\right] - \frac{3zx^2}{\rho^5}\right\} \tag{A.1}$$

$$\tau_{xz}^n = -\frac{3F_N}{2\pi}\cdot\frac{xz^2}{\rho^5} \tag{A.2}$$

The tangential force (F_T)-induced Cerruti field is given by

$$\sigma_x^t = -\frac{F_T}{2\pi}\left\{\frac{3x^3}{\rho^5}-(1-2\nu)\left[\frac{x}{\rho^3}-\frac{3x}{\rho(\rho+z)^2} + \frac{x^3}{\rho^3(\rho+z)^2}+\frac{2x^3}{\rho^2(\rho+z)^3}\right]\right\} \tag{A.3}$$

$$\tau_{xz}^t = -\frac{F_T}{2\pi}\cdot\frac{3x^2z}{\rho^5} \tag{A.4}$$

where $r^2 = x^2+y^2$, $\rho^2 = x^2+y^2+z^2$, $z = a_c$ [33], and ν is the Poisson ratio.

The residual stress-induced sliding blister field is represented by

$$\sigma_x^r = \frac{2B}{\left(y^2+z^2\right)^2}\cdot\left\{-2\nu\left(y^2-z^2\right)+\frac{x}{\rho^5}\right.$$
$$\times\left(2\nu x^4y^2-2x^2y^4+6\nu x^2y^4-2y^6\right.$$
$$+4\nu y^6-2\nu x^4z^2-4x^2y^2z^2+2\nu x^2y^2z^2$$
$$-3y^4z^2+6\nu y^4z^2-2x^2z^4$$
$$\left.\left.-4\nu x^2z^4+z^6-2\nu z^6\right)\right\} \quad (A.5)$$

$$\tau_{xz}^r = -\frac{2B\cdot z}{\rho^5}\left(2x^2+2y^2-z^2\right) \quad (A.6)$$

where B is the strength of the blister field per unit length. This is determined by

$$B = F_N\cdot f\frac{E}{H}\frac{3\lambda^2}{4\pi^2(1-2\nu)(1+\nu)}\frac{a_c}{h} \quad (A.7)$$

where E is the Young' s modulus, H is the hardness, λ is the geometric factor ($\lambda = 1$ for the axisymmetric tool, e.g. conical tool [34]), and f is the compaction factor, which is equal to the ratio of the elastically accommodated volume of the burnished groove to the deformation volume during the burnishing process [34]. Thus, the compaction factor is given by

$$f = \left(A_s - A_r\right)/A_s \quad (A.8)$$

where A_r is the residual cross-sectional area of the burnished groove, and A_s is the cross-sectional area of the burnished groove during the burnishing process. By calculating the areas of cross-sectional profiles obtained using AFM, for example, the f at the normal force of 10 mN under dry and lubricated conditions are 0.527 and 0.556, respectively.

References

[1] J. Yan, K. Maekawa, J. Tamaki, T. Kuriyagawa, Micro grooving on single-crystal germanium for infrared Fresnel lenses, J. Micromech. Microeng. 15 (2005) 1925–1931.
[2] Q. Liu, Z. Liao, D. Axinte, Temperature effect on the material removal mechanism of soft-brittle crystals at nano/micron scale, Int. J. Mach. Tool Manufact. 159 (2020) 103620.
[3] J. Zhang, J. Shi, D. Qi, L. Chen, K.H.L. Zhang, Recent progress on the electronic structure, defect, and doping properties of Ga2O3, Apl. Mater. 8 (2020), 020906.
[4] S. Zhang, X. Guo, Z. Jin, R. Kang, D. Guo, Material removal characteristics of precorroded Lu2O3 laser crystals and elastic deformation model during nanoscratch process, Tribol. Int. 143 (2020) 106027.
[5] R. Komiya, T. Kimura, T. Nomura, M. Kubo, J. Yan, Ultraprecision cutting of single-crystal calcium fluoride for fabricating micro flow cells, Journal of Advanced Mechanical Design, Systems, and Manufacturing 12 (2018) JAMDSM0021.
[6] E.M. Gavrushchuk, Polycrystalline zinc selenide for IR optical applications, Inorg. Mater. 39 (2003) 883–899.
[7] E.K. Antwi, K. Liu, H. Wang, A review on ductile mode cutting of brittle materials, Front. Mech. Eng. 13 (2018) 251–263.
[8] S. Azami, H. Kudo, Y. Mizumoto, T. Tanabe, J. Yan, Y. Kakinuma, Experimental study of crystal anisotropy based on ultra-precision cylindrical turning of single-crystal calcium fluoride, Precis. Eng. 40 (2015) 172–181.
[9] J.D. Owen, J.R. Troutman, T.A. Harriman, A. Zare, Y.Q. Wang, D.A. Lucca, M. A. Davies, The mechanics of milling of germanium for IR applications, CIRP Annals 65 (2016) 109–112.
[10] S. Gao, Y. Wu, R. Kang, H. Huang, Nanogrinding induced surface and deformation mechanism of single crystal β-Ga2O3, Mater. Sci. Semicond. Process. 79 (2018) 165–170.
[11] B. Swennen, A. Mallants, H.A. Roels, J.P. Buchet, A. Bernard, R.R. Lauwerys, D. Lison, Epidemiological survey of workers exposed to inorganic germanium compounds, Occup. Environ. Med. 57 (2000) 242–248.
[12] National Center for Biotechnology Information, PubChem Compound Summary for CID 516951, Potassium Dihydrogen Phosphate, 2020. https://pubchem.ncbi.nlm.nih.gov/compound/Potassium-dihydrogen-phosphate. (Accessed 16 September 2020).
[13] R.K. Wolff, R.F. Henderson, A.F. Eidson, J.A. Pickrell, S.J. Rothenberg, F.F. Hahn, Toxicity of gallium oxide particles following a 4-week inhalation exposure, J. Appl. Toxicol. 8 (1988) 191–199.
[14] National Center for Biotechnology Information, PubChem Compound Summary for CID 159406, Lutetium Oxide (Lu2O3), 2020. https://pubchem.ncbi.nlm.nih.gov/compound/Lutetium-oxide-_Lu2O3. (Accessed 16 September 2020).
[15] National Center for Biotechnology Information, PubChem Compound Summary for CID 84512, Calcium Fluoride, 2020. https://pubchem.ncbi.nlm.nih.gov/compound/Calcium-fluoride. (Accessed 16 September 2020).
[16] National Center for Biotechnology Information, PubChem Compound Summary for CID 4298215, Zinc Selenide (ZnSe), 2020. https://pubchem.ncbi.nlm.nih.gov/compound/Zinc-selenide-_ZnSe. (Accessed 16 September 2020).
[17] M. Korzynski, J. Lubas, S. Swirad, K. Dudek, Surface layer characteristics due to slide diamond burnishing with a cylindrical-ended tool, J. Mater. Process. Technol. 211 (2011) 84–94.
[18] M. Korzynski, Modeling and experimental validation of the force-surface roughness relation for smoothing burnishing with a spherical tool, Int. J. Mach. Tool Manufact. 47 (2007) 1956–1964.
[19] F.L. Li, W. Xia, Z.Y. Zhou, J. Zhao, Z.Q. Tang, Analytical prediction and experimental verification of surface roughness during the burnishing process, Int. J. Mach. Tool Manufact. 62 (2012) 67–75.
[20] A. Teramachi, J. Yan, Improving the surface integrity of additive-manufactured metal parts by ultrasonic vibration-assisted burnishing, J. Micro Nano-Manufacturing 7 (2019).
[21] S.E. Grillo, M. Ducarroir, M. Nadal, E. Tourni, J. Faurie, Nanoindentation of Si, GaP, GaAs and ZnSe single crystals, J. Phys. Appl. Phys. 36 (2002) L5–L9.
[22] I. Yonenaga, K. Watanabe, S. Itoh, S. Fujiwara, Dynamics and characters of dislocations in ZnSe, J. Mater. Sci. 41 (2006) 2601–2604.
[23] C. Pu, L. Dai, H. Li, H. Hu, K. Liu, L. Yang, M. Hong, Pressure-induced phase transitions of ZnSe under different pressure environments, AIP Adv. 9 (2019), 025004.
[24] E.M. Gavrishchuk, É.V. Yashina, Zinc sulfide and zinc selenide optical elements for IR engineering, J. Opt. Technol. 71 (2004) 822–827.
[25] L. Huang, C. Bonifacio, D. Song, K.V. Benthem, A.K. Mukherjee, J.M. Schoenung, Investigation into the microstructure evolution caused by nanoscratch-induced room temperature deformation in M-plane sapphire, Acta Mater. 59 (2011) 5181–5193.
[26] S. Stephan, M. Dyga, H.M. Urbassek, H. Hasse, The influence of lubrication and the solid-fluid interaction on thermodynamic properties in a nanoscopic scratching process, Langmuir 35 (2019) 16948–16960.
[27] Y. Wang, D. Raabe, C. Klüber, F. Roters, Orientation dependence of nanoindentation pile-up patterns and of nanoindentation microtextures in copper single crystals, Acta Mater. 52 (2004) 2229–2238.
[28] E. Brinksmeier, W. Preuss, O. Riemer, R. Rentsch, Cutting forces, tool wear and surface finish in high speed diamond machining, Precis. Eng. 49 (2017) 293–304.
[29] J. Yan, Y. Takahashi, J. Tamaki, A. Kubo, T. Kuriyagawa, Y. Sato, Ultraprecision machining characteristics of poly-crystalline germanium, JSME International Journal Series C Mechanical Systems, Machine Elements and Manufacturing 49 (2006) 63–69.
[30] W. Huang, J. Yan, Surface formation mechanism in ultraprecision diamond turning of coarse-grained polycrystalline ZnSe, Int. J. Mach. Tool Manufact. 153 (2020) 103554.

[31] D. Xia, X. Chen, G. Huang, B. Jiang, A. Tang, H. Yang, S. Gavras, Y. Huang, N. Hort, F. Pan, Calculation of Schmid factor in Mg alloys: influence of stress state, Scripta Mater. 171 (2019) 31–35.
[32] J.R. Luo, A. Godfrey, W. Liu, Q. Liu, Twinning behavior of a strongly basal textured AZ31 Mg alloy during warm rolling, Acta Mater. 60 (2012) 1986–1998.
[33] Y. Ahn, T.N. Farris, S. Chandrasekar, Sliding microindentation fracture of brittle materials: role of elastic stress fields, Mech. Mater. 29 (1998) 143–152.
[34] X. Jing, S. Maiti, G. Subhash, A new analytical model for estimation of scratch-induced damage in brittle solids, J. Am. Ceram. Soc. 90 (2007) 885–892.
[35] K. Wasmer, M. Parlinska-Wojtan, S. Graça, J. Michler, Sequence of deformation and cracking behaviours of Gallium–Arsenide during nano-scratching, Mater. Chem. Phys. 138 (2013) 38–48.
[36] P. Zhu, Y. Hu, T. Ma, H. Wang, Molecular dynamics study on friction due to ploughing and adhesion in nanometric scratching process, Tribol. Lett. 41 (2011) 41–46.
[37] S. Lafaye, C. Gauthier, R. Schirrer, The ploughing friction: analytical model with elastic recovery for a conical tip with a blunted spherical extremity, Tribol. Lett. 21 (2006) 95–99.
[38] C. Li, F. Zhang, Y. Wu, X. Zhang, Influence of strain rate effect on material removal and deformation mechanism based on ductile nanoscratch tests of Lu2O3 single crystal, Ceram. Int. 44 (2018) 21486–21498.
[39] G. Garcia Luna, D. Axinte, D. Novovic, Influence of grit geometry and fibre orientation on the abrasive material removal mechanisms of SiC/SiC Ceramic Matrix Composites (CMCs), Int. J. Mach. Tool Manufact. 157 (2020) 103580.
[40] B. Cheng, H. Lou, A. Sarkar, Z. Zeng, F. Zhang, X. Chen, L. Tan, V. Prakapenka, E. Greenberg, J. Wen, R. Djenadic, H. Hahn, Q. Zeng, Pressure-induced tuning of lattice distortion in a high-entropy oxide, Communications Chemistry 2 (2019) 114.
[41] Y.Q. Wu, H. Huang, J. Zou, Lattice bending in monocrystalline GaAs induced by nanoscratching, Mater. Lett. 80 (2012) 187–190.
[42] D. Mergel, Z. Qiao, Correlation of lattice distortion with optical and electrical properties of In2O3:Sn films, J. Appl. Phys. 95 (2004) 5608–5615.
[43] K. Kosai, J. Yan, Effects of cyclic loading on subsurface microstructural changes of zirconia polycrystals in nanoscale mechanical processing, Int. J. Mach. Tool Manufact. 159 (2020) 103626.
[44] S.I. Wright, M.M. Nowell, D.P. Field, A review of strain analysis using electron backscatter diffraction, Microsc. Microanal. 17 (2011) 316–329.
[45] A. Kundu, D.P. Field, Influence of plastic deformation heterogeneity on development of geometrically necessary dislocation density in dual phase steel, Mater. Sci. Eng. 667 (2016) 435–443.
[46] M.A. Rahman, M.R. Amrun, M. Rahman, A.S. Kumar, Variation of surface generation mechanisms in ultra-precision machining due to relative tool sharpness (RTS) and material properties, Int. J. Mach. Tool Manufact. 115 (2017) 15–28.
[47] H. Xiao, R. Liang, O. Spires, H. Wang, H. Wu, Y. Zhang, Evaluation of surface and subsurface damages for diamond turning of ZnSe crystal, Optic Express 27 (2019) 28364–28382.
[48] S. Zhang, Y. Zhou, H. Zhang, Z. Xiong, S. To, Advances in ultra-precision machining of micro-structured functional surfaces and their typical applications, Int. J. Mach. Tool Manufact. 142 (2019) 16–41.